Photocatalytic Hydrogen Production

by Clare Ann Morton

in partial fulfilment of the requirements for the degree

Master of Philosophy in Chemistry

Cardiff University

2014

"And what will they burn instead of coal?" asked Pencroft.

"Water," replied Harding. "But water decomposed into its primitive elements… yes my friends, I believe that water will one day be employed as fuel, that hydrogen and oxygen which constitute it will furnish an inexhaustible source of heat and light. Water will be the coal of the future."

Jules Verne, **The mysterious island**, *1874*

Acknowledgements

Abstract

The photocatalytic methanol reforming reaction has been studied using many different Pd/Pt loaded TiO_2 powdered catalysts, focussing on the effect of weight loading and reaction phase on the rate of hydrogen production. The palladium/platinum weight loading dependence in the gas and liquid phase showed that independent of the phase of reaction, the amount of hydrogen produced from methanol reforming irradiated by UV light decreased for increasing metal weight loading. Further studies were conducted to test the reactivity of rutile and anatase phase titania supported palladium/platinum catalysts for their ability to produce hydrogen in the methanol reforming reaction, both phases were found to be poor photocatalysts alone but upon combination both chemically in the P25 based catalysts and in physical mixtures, where Pd was present on only the rutile phase, the amount of hydrogen produced was improved.

The reactivity of surface oxygen and crotonaldehyde has also been studied under ultra-high vacuum (UHV) conditions on Pd (110). Key UHV techniques employed included molecular beam sticking, X-ray photoelectron spectroscopy (XPS). Adsorbed oxygen was found to migrate into the bulk following molecular beam experiments where the period between incident beam exposure on the Pd crystal was altered over time. For the crotonaldehyde molecular beam experiments decarbonylation was observed for ambient reaction temperatures and dehydrogenation was observed at elevated temperatures.

Successful palladium growth by the Volmer-Weber island growth mode were reported for the production of a model Pd/TiO_2 (110) catalyst via metal vapour deposition (MVD) however surface palladium concentration was too low for molecular sticking reactions to be carried out on the surface

Contents

Chapter sections and their associated page numbers are described on the contents page at the beginning of each chapter.

Chapter 1 – Introduction

Contents

1   General

Humankind's ability to manipulate fuel sources to release useful energy has been an integral part of our civilisations evolution. However this has led to us being heavily reliant upon fossil fuels, for example in 2002 it was predicted that 80 % of global energy demands were met by fossil fuels[1]. As the human population continues to grow the demand for energy will rise and will contribute further towards the depletion of the finite fossil fuel reserves which support us. The use of fossil fuels has escalated to a global energy situation, in which there are four main areas of concern; depletion of fossil fuels, global warming, rising energy costs and energy security[2].

With this in mind it is not surprising that there is a growing need for alternative high energy fuels alongside continuing development of other renewable energy supplies such as, wind, solar and tidal. Ideally these potential fuels of the future would also have no damaging effect on our atmosphere, whilst having a usable energy density and being economically viable[3]. In addition to this if the fuel were to use available technology that is useable on a local basis, this would also factor out concerns over energy security and in theory eradicate any energy situation that may develop.

Hydrogen produced via photocatalysis from water would be a suitable answer to these problems[4]. In addition, hydrogen has an extremely high energy output per unit mass[3]; almost three times more than petrol; conveniently there is an abundant source of hydrogen at our disposal, in the form of water which covers over 70 % of the Earth's surface, not to mention that complete combustion of hydrogen will regenerate water[5] (Eq^n 1.1) and therefore give no unwanted products, which linking back to the original concerns mentioned related to fossil fuels would not contribute towards global warming. Furthermore, generating hydrogen by photocatalysis is a superb way of utilising the solar energy reaching the Earth's surface.

$$H_2 + \tfrac{1}{2}\, O_2 \leftrightarrow H_2O \qquad\qquad \textbf{(Eq}^n\textbf{ 1.1)}$$

1.1 Heterogeneous Catalysis

To recognise the potential of using photocatalysis as a source of hydrogen production one must take a step back and consider the underlying principles of catalysis and its role in chemistry. Catalysis occurs in many walks of life, high up in the atmosphere, in the destruction of the ozone to the insides of all living creatures in enzynamitc catalytic processes, for all these thousands of systems, a catalyst of some description will act to reduce the activation barrier of reactants to products, accelerating the rate of reaction for the system in question, without being consumed. This process is displayed schematically in Figure 1.1. There are two main divisions of catalysis, namely homogeneous and heterogeneous, the latter phase is the most frequently employed technique used in industrial processes. The difference between the two types of catalysis is embodied and described by their respective titles, where homogeneous catalysis, implies that the catalyst and reactants are in the same chemical phase and by association, the catalyst and reactants are in a different chemical phase to each other in heterogeneous catalysis.
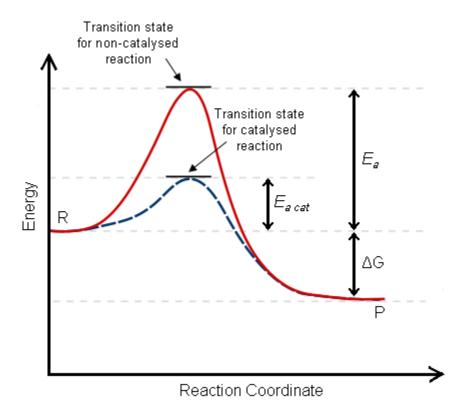

Figure 1.1: Schematic representation of how a catalyst works by lowering the activation energy of a reaction.

It is most common for the catalyst to be in the solid state and the reactants to be in either the liquid or gas phase in industrial scale processes that employ heterogeneous catalysis, an everyday example of one of these processes, would be the control of exhaust emission via the catalytic converter used in a car. For heterogeneous catalysis, the interaction of reactants with the catalyst surface is of particular importance and as such is a recurring topic of investigation in the ever-increasing interest displayed in this field of chemistry.

Despite the wave of research concerning this area in the past half century, curiosity in this field originated back in the early 19th century, with the development of the Davy lamp originating from studies into the reactivity of coal gas and air mixtures on heated platinum wires[6]. It was not until almost twenty years later however that Berzelius[7], penned a definition for catalysis, following more studies into the reaction of gases with Pt surfaces, namely those conducted by Dobereiner[8]. Several large scale industrial catalytic processes were engineered before the turn of the 20th century, including, chlorine and hydrogen production. Development of improved catalysts to increase the yield and selectivity of reactions came to a pinnacle in the early 20th century, with the introduction of an iron based catalyst in the production of ammonia from hydrogen and nitrogen, a process which is still employed today to produce a third of the world's fertilizer, this catalytic system is known as the Haber process[9]. Several other large scale industrial processes, which are still in use today, include the cracking and reforming of oil into several crucial products, namely petrol and diesel for use as fuel and production of molecules such as ethylene and propylene for large scale polymer production. In essence catalysis provides the back bone to industrial processes that humankind has become reliant upon and it is only through more detailed understanding of the surface level mechanism at play that improvements can be made to the catalysts employed in these systems.

1.2   Photocatalysis

Employing catalysis to lower the activation energy required in the dehydrogenation of water to produce hydrogen as a viable and stainable source of energy for combustion is a valid procedure, but this will only reduce the kinetics involved whereas the major setback in the

production of hydrogen in this way is the thermodynamics involved, since water is an extremely stable element, and consequently releasing its molecular building blocks is a very endothermic process, as represented in Figure 1.2. Therefore a large energy input is required to fulfil the overall energy demand of this process, for example thermal decomposition requires temperatures between 2400 $^{\circ}$C and 3200 $^{\circ}$C [10] to achieve a majority conversion of water to oxygen and hydrogen gas.

Energy/

$$O_{(g)} \quad + \quad 2H_{(g)}$$

681.4 ———

426.3 kJmol^{-1}

-433.7 kJmol^{-1}

$$H_{(g)} + OH_{(g)}$$

$$O_{(g)} + H_{2\,(g)}$$

255.1 ———

-247.7 kJmol^{-1}

494.8 kJmol^{-1}

$$\tfrac{1}{2} O_{2\,(g)} + H_{2\,(g)}$$

0 ———

$$H_2O_{(g)}$$

-239.7 ———

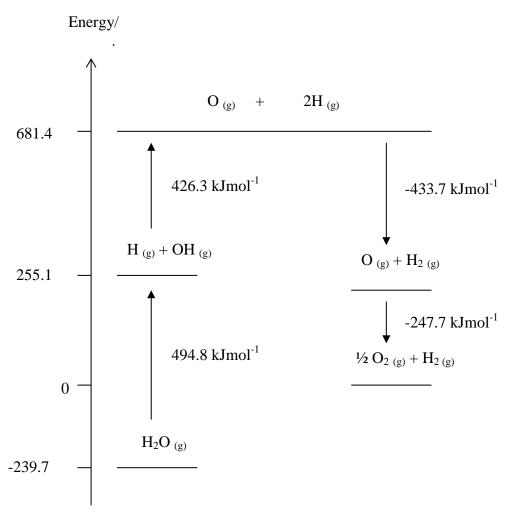**Figure 1.2: The energetics of direct water splitting.**

However, sunlight energy is an alternative energy source available to overcome the thermodynamic difficulties encountered during water splitting. Figure 1.3 shows the spectral irradiance present on the Earth's surface with respect to wavelength, photons with a wavelength of 500 nm or lower (assuming 100 % light conversion) have sufficient energy to

bridge this thermodynamic barrier and as the solar spectrum shows, are present in the visible region of the spectrum.

Water is stable on the Earth's surface though, due to the additional kinetic barrier, which prevents the world's water resources from being reduced to hydrogen and oxygen. The kinetic barrier arises due to the high energy input ~500 kJmol^{-1} required to break the first H-O bond, this energy translates to a wavelength of <250 nm and is shown as a blue line on the solar spectrum in Figure 1.3. Light energy of this wavelength is filtered out in the atmosphere and hence is not abundant at the Earth's surface, which is fortunate for humankinds demand for water as a life source but problematic in the search for a new fuel source.
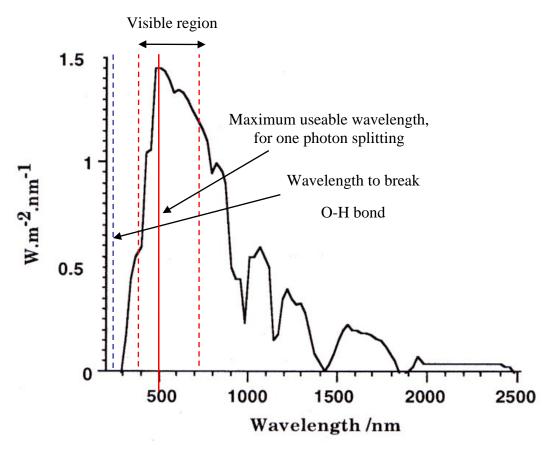
Figure 1.3: Solar spectrum on Earth, with single photon water splitting thresholds shown. Detailing the solar energy intensity (Wm^{-2}nm^{-1}) detected for each region of the solar spectrum on Earth. The most intense region of the solar spectrum experienced on Earth corresponds to the visible region which makes up46 % light intensity.

Currently, catalysis is a solution to lower the activation energy required to overcome the large kinetic barrier that prevents water splitting from occurring naturally and enabling us to utilise visible/uV radiation to initiate water splitting reaction rather than the high energy radiation, which is required in the un-catalysed reaction and is not present in the Earth's atmosphere.

Through a combination of sunlight and catalysis, photocatalysis, the thermodynamic and kinetic constraints incurred during hydrogen production can be managed. The model material for this purpose would provide both the catalytic and photo absorption function, a semiconductor is a suitable material that meets these requirements, namely having a bandgap, E_g, in the visible range, with $E_g \sim 250$ kJ mol^{-1} (~2.4 eV) equivalent to the energy of photons in visible light. For a semiconductor with a bandgap in the range of 2.4 eV, this would mean that visible light photons absorbed by the material will have enough energy to promote electrons from the valence band of the semiconductor to the conduction band, creating an electron/hole pair, described in Eq 1.2.

$$\text{Semiconductor} + h\upsilon \rightarrow e^-_{cb} + h^+_{vb}$$
Eq^n 1.2

The photogenerated electron/hole pair provides both a reductive and oxidative site to produce hydrogen and oxygen, respectively, from water. The simultaneous presence of reduction and oxidation at the semiconductor surface needs to be included when deciding upon a suitable semiconductor for use in these reactions, a list of several semiconductors, with appropriate band gaps, has been put together by Gratzel[11] and can be seen in Figure 1.4.
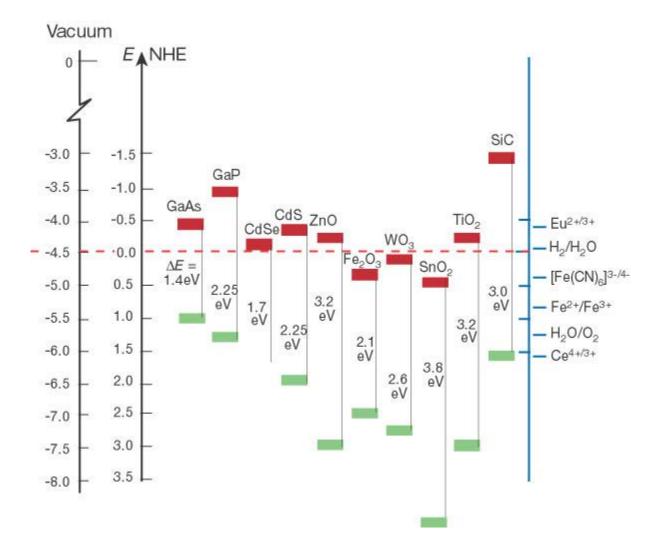
Figure 1.4: Band positions of several semiconductors in contact with aqueous electrolyte at pH 1, adapted from Gratzel[11]. Red bar represents the lower level of the conduction band and the green bar represents the upper edge of the valence band, the corresponding band gap is detailed in electron volts between these bands. The energy scale is indicated in electron volts using either the normal hydrogen electrode (NHE) or the vacuum level as a reference. The right hand scale (blue line) shows the standard potentials of several redox couples are presented against the standard hydrogen electrode potential.

Figure 1.4, shows several semiconductors that meet the criteria needed to utilise light energy in photocatalysis, for the purpose of this research titanium dioxide, TiO_2, has been chosen, although CdS and ZnO have also been proven as successful photocatalyst supports[12]. Both CdS and ZnO supports have a suitable bandgap for electron/hole generation from visible light photons; however these supports undergo degradation by the very same photo-generated holes needed for hydrogen production from water, requiring the addition of sacrificial electron donors. Titania on the other hand does not undergo photo-degradation; however TiO_2 does have a slightly higher energy bandgap, 3.2 eV, which means that it can only absorb

photons from the ultra violet range of the solar spectrum experienced on Earth. Further arguments for the use of titania as a semiconductor support for the photocatalytic production of hydrogen include its availability and non-toxicity.

The addition of a transition metal supported on a suitable semiconductor introduces an "electron sink" to prevent the immediate recombination of the electron/hole pairs created by the photon interaction with the semiconductor valence band. Several ways to increase the lifetime of electron/hole pairs have been investigated, including the introduction of electron mediators to a reaction system, for example methyl viologen[13] (1,1'-Dimethyl-4-4'-bipyridinium dichloride, MV^{2+}), Fe^{+3}/Fe^{+2} systems[14] and IO_3^-/i^- systems[15]. Another technique for increasing the electron/hole lifetime of the semiconductor, in particularly TiO_2, is by noble metal loading, a practice that will be employed in the study detailed here. Over the years, Pt, Au, Pd, Rh, Ni, Cu and Ag have all been reported to enhance photocatalysis on TiO_2[16-31]. The Fermi level for these transition metals is lower than titania's, meaning that photogenerated electrons are able to transfer from the semiconductor to the transition metal at the surface of the catalyst, creating an "electron sink", which in turn prevents electron/hole recombination. Transition metal loading and rare earth metal loading have also been attributed to lowering the band gap of the titania support and hence increasing the photo-response of titania catalysts shifting their absorbance properties from the UV region to the visible region, a concise review of these metals and their effect on hydrogen production by titania catalysts has been produced by Meng Ni et al[32].

As a consequence of lowering the activation energy, the energy required for the recombination of the separated hydrogen and oxygen will also reduce and increase the likelihood of back reaction and result in a lowering of the overall yield, introducing the need for an indirect route to hydrogen production using light energy, by the use of physical mixtures of organic sacrificial agents and water in photocatalytic reforming reactions. The addition of sacrificial agents in the reaction pot could overcome this problem by providing a reaction route to remove the unwanted O_2 products from the reaction mixture and prevent the back reaction from occurring. The important features of reforming mixtures of water and organic molecules to produce hydrogen are that they can be exploited under ambient conditions and require relatively low tech chemical methods to report successful yields, when compared directly to thermochemical processes such as steam reforming of methanol. Several studies have also been conducted into the use of products that can be derived from biomass

for use as sacrificial agents in the photocatalytic reforming process, for example, ethanol, glycerol[33], glucose, sucrose[34, 35], starch and wood[36] and even sewage sludge[37]!

Over the past few decades' production of hydrogen via catalysis using sunlight as an energy source has become a major investment in scientific research. The high Gibbs free energy required to initiate direct water splitting has led to the indirect routes using the techniques described above being investigated, including reforming reactions of organic compounds. The work within the Bowker group and presented here focuses on methanol reforming to produce hydrogen by photocatalysis and will be described in more detail in chapter three.

1.3   The Surface Science Approach to Catalysis

For heterogeneous catalysis, the interaction of reactants with the catalyst surface is of particular importance affecting the overall efficiency of the catalytic process. Surface additives on a catalyst can either enhance or hinder a particular reaction; these interactions are governed by features of the surface layer of atoms and can be used to determine how fast a catalytic reaction will take place and consequently influence the reaction taking place at the catalyst surface. Advancement in the disciplines of ultra-high vacuum (UHV) and solid state physics over the past century, significantly the work pioneered Irving Langmuir[38, 39], has allowed studies to be conducted at an atomic scale, making headway for surface specific definitions used to describe and hence understand catalytic cycles at a surface/molecular scale, namely the differences between physisorption and chemisorption[40, 41].   The development of multiple new surface specific techniques in the last half of the 21st century has accelerated the growth in surface science and its uses in understanding the underlying mechanisms of a reaction, notably scanning tunnelling microscopy (STM)[42 43], low energy electron diffraction (LEED)[44] and atomic force microscopy (AFM)[45]. By employing these techniques it is possible to build an advanced understanding of the mechanistic details with regards to surface reactions as scientists are able to directly image possible adsorption sites and atomic scale surface features and defects.

The complexity and unique structure present at the surface of a 'rough' solid at an atomic level, with each individual deviation from uniformity at the surface lending different electronic properties, contributes towards the irreproducibility of a catalyst's surface

composition to study. Therefore to undergo reproducible experimentation into the properties of a catalyst and how its surface behaviour influences a reaction, one must revert back to a simplified system in order to build upwards to propose the mechanism at play. By employing a well-defined surface, created by cutting through a crystal at a particular crystal plane, the complexity displayed at the surface of a 'rough' solid can be introduced by adding controlled amounts of surface defects and coverages of distinguishable adsorbates, to create a model environment.
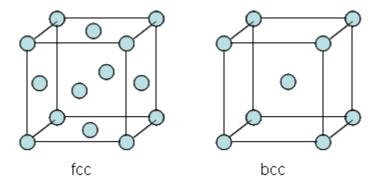

fcc   bcc

Figure 1.5: An illustration of the fcc and bcc lattice structures.

Miller indices are used to describe the model environment of well-defined surfaces, exposed upon cutting a crystal in a given orientation, these miller indices are directly related to the positions of the atoms in the bulk lattice. Figure 1.5 illustrates the common bulk lattices that most transition metals commonly form, either face-centred cubic (fcc) or body-centred cubic (bcc) structures. Silver, gold, copper, palladium, platinum and nickel are all examples of metals that form a close packed fcc structure, while iron, molybdenum and tungsten are examples of bcc structures. Figure 1.6 schematically details the surface structure, which would be present upon slicing an fcc class of solid through the (110), (100) and (111) Miller index faces. Each Miller index structure gives rise to its own coordination of atoms; surfaces with lower coordination surface atoms have the highest free energy available for adsorption. For the miller indices described here for the reactivity of fcc structures can be shown to be $(110) > (100) > (111)$.
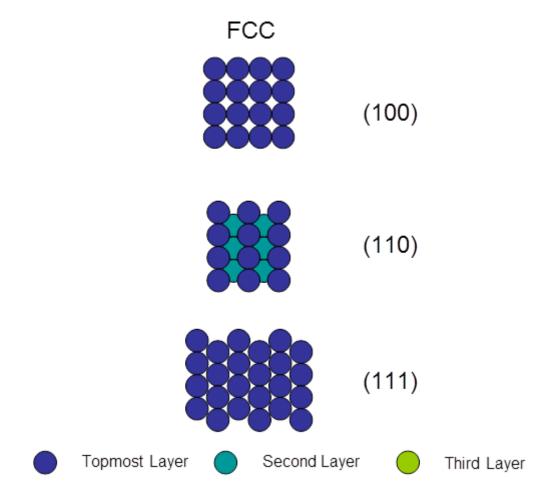
Figure 1.6: The (100), (110) and (111) atomic surface structures for fcc crystals.

The single crystal work presented in this thesis will focus upon two single crystals, to describe the model catalyst used within the photocatalytic methanol reforming system. The simpler low coordination Pd (110) and a more complex TiO_2 (110) single crystal due to the presence of two atoms in the bulk make-up of the crystal, Figure 1.7 exemplifies the lattice structure of bulk titania. Surface free energy calculations have shown the rutile (110) phase of titania to be the most stable crystal face[46].
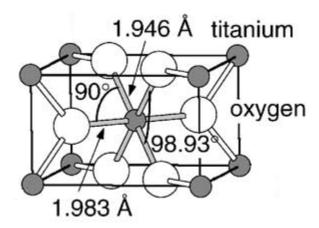
Figure 1.7: The tetragonal bulk unit cell of rutile titania. Slightly distorted octahedra are the basic building units and the bond lengths and angles of the octahedrally coordinated Ti atoms are indicated. Image taken from a review paper by U. Diebold[47]

A simplified ball and stick model of the surface structure of a pristine TiO_2 (110) surface, which exhibits the (1 x 1) bulk termination is shown in Figure 1.8. In this structure, the titanium atoms exist solely in the Ti^{2+} oxidation state whilst the uppermost oxygen atoms are referred to as bridging oxygen's. It is these oxygen atoms that are commonly removed under certain reaction conditions, resulting in an overall reduction of the titania single crystal, which, in turn, directly influences the surface properties.
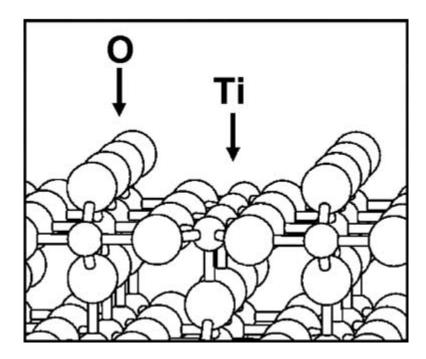
Figure 1.8: A ball and stick model of the (1 x 1) bulk terminated TiO$_2$ (110) surface. The oxygen atoms indicated in the diagram are referred to as bridging oxygen's.

Figure 1.9 schematically shows the easily identifiable adsorbate sites for a low energy surface (110) fcc crystals, bonding can occur directly on top of a surface atom (one-fold), bridging two adjacent atoms (two-fold) or in a hollow (four-fold). For a (110) fcc crystal there are two types of bridging; short bridge bonding between atoms in the same row and long bridge bonding between atoms in different rows. The relatively simple differences between the adsorption sites illustrated in Figure 1.9 can result in a significant variation in the way a molecule adsorbs and subsequently reacts with a surface, thus exemplifying the fact that the surface arrangement of atoms directly influences the behaviour and reactive properties of a given substrate.
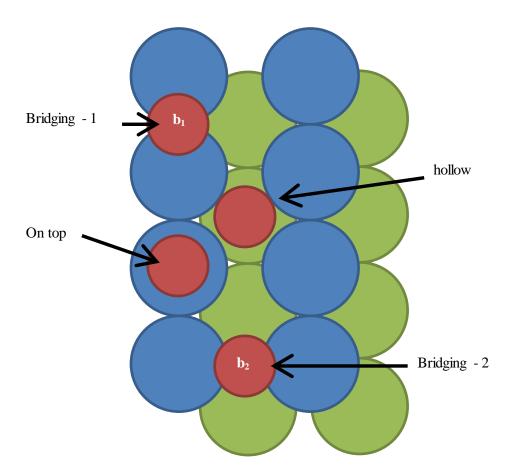
Figure 1.9: The four possible adsorption sites for a gaseous reactant on an (110) fcc crystal surface.

Understanding the basic mechanism of adsorption which is occurring at a surface has been employed in the studies of many photocatalytic systems, notably the role that palladium catalysts adopt in three way automotive catalytic converters has been intensively studied using simple Pd single crystals under UHV conditions. Surface level studies into the oxidation of CO to CO_2[48-50] and the reduction of NO_x species into less harmful nitrogen based products[51-53] have directly influenced the continued development of three-way catalytic convertors, allowing them to become more efficient at the reactions they perform.

Similar surface studies will be applied in this study to try and aid our understanding of the mechanism at play in the photocatalytic methanol reforming reaction.

1.4 Aims and Thesis Outline

The body of work presented here will look to investigate both fundamental and applied aspects of hydrogen production from sunlight using photocatalytic technology. The experiments conducted here will specifically focus upon the production of hydrogen from water/methanol reforming systems, employing photocatalysts made up of transition metals loaded upon different titania phase supports.

This introduction chapter, chapter one, has provided a solid background to heterogeneous catalysis and how the features of these catalysts, which have embedded themselves into essential processes used within the chemical industries today, will provide useful insight into reducing the energy barrier witnessed in hydrogen production from water. The chapter has also included discussion of the factors, which influence photocatalysis and how the surface science approach can be utilised to understand the mechanism of a reaction and consequently adapted to improve catalyst performance.

An experimental chapter, chapter two, documents the photocatalyst techniques used, including the production of powdered catalysts, equipment and calculations used in the following results chapter. The nature of the UHV apparatus and conditions utilised is also described in detail in chapter two, with in depth background theory for the surface science techniques used in this research which aids the understanding of the experiments performed in the final results chapters.

Chapter three will concentrate on producing photocatalysts by classical chemical routes and measuring the reactivity with a photo-reactor. Focus will be paid towards the effect of Pd and Pt metal weight loading on P25 titania supports and the dependence of the crystallite phase of the titania pre-cursor to determine how these factors contribute towards the hydrogen production in the photocatalysised methanol reforming reaction. The photocatalytic system will also be tested for its ability to produce hydrogen using a different sacrificial organic agent, crotonaldehyde.

On the fundamental side surface science methods, mainly molecular beam experiments and x-ray photoelectron spectroscopy will be used to investigate model aspects of the photocatalytic system. Investigating the reactivity of adsorbed oxygen on the surface of model Pd(110) catalysts and crotonaldehyde, to relate the applied ability demonstrated by

crotonaldehyde in chapter three to a model catalyst system. The fabrication of Pd nanoparticles and the nature of their growth onto TiO_2 (110) single crystal surface will be described.

Chapter five concludes the body of work conducted here; giving a general summary of the findings of the experiments performed in chapter's three and four.

1.5 References

1.   IEA., Internationl energy agency statistics, 2002.

2.   M. Asif and T. Muneer, *Renewable & Sustainable Energy Reviews*, 2007, **11**, 1388-1413.

3.   T. N. Veziroglu and F. Barbir, *International Journal Hydrogen Energy*, 1992, **17**, 391-404.

4.   M. Bowker, L. Millard, J. Greaves, D. James and J. Soares, *Gold Bulletin*, 2004, **37**, 170-173.

5.   A. J. Bard and M. A. Fox, *Accounts of Chemical Research*, 1995, **28**, 141-145.

6.   H. Davy, *Philosophical Transactions of the Royal Society of London*, 1817, **107**, 77-85.

7.   J. Berzelius, *Royal Swedish Academy of Sciences*, 1835.

8.   J. Döbereiner, *Annalen der Physik* 1836, **74**, 269.

9.   F. Haber, *Angewandte Chemie*, 1914, **27**, 473-477.

10.   J. Lédé, F. Lapicque and J. Villermaux, *International Journal of Hydrogen Energy*, 1983, **8**, 675-679.

11.   M. Grätzel, *Nature*, 2001, **414**, 338-344.

12.   M. Kosanić and A. Topalov, *International Journal of Hydrogen Energy*, 1990, **15**, 319-323.

13.   J. R. White and A. J. Bard, *The Journal of Physical Chemistry*, 1985, **89**, 1947-1954.

14.   Y. Sasaki, A. Iwase, H. Kato and A. Kudo, *Journal of Catalysis*, 2008, **259**, 133-137.

15.   H. Kotani, T. Ono, K. Ohkubo and S. Fukuzumi, *Physical Chemistry Chemical Physics*, 2007, **9**, 1487-1492.

16.   N.-L. Wu and M.-S. Lee, *International Journal of Hydrogen Energy*, 2004, **29**, 1601-1605.

17.   M. R. St. John, A. J. Furgala and A. F. Sammells, *The Journal of Physical Chemistry*, 1983, **87**, 801-805.

18.   G. R. Bamwenda, S. Tsubota, T. Nakamura and M. Haruta, *Journal of Photochemistry and Photobiology a-Chemistry*, 1995, **89**, 177-189.

19.   M. Jakob, H. Levanon and P. V. Kamat, *Nano Letters*, 2003, **3**, 353-358.

20.   S. Jin and F. Shiraishi, *Chemical Engineering Journal*, 2004, **97**, 203-211.

21. P. V. Kamat, M. Flumiani and A. Dawson, *Colloids and Surfaces a-Physicochemical and Engineering Aspects*, 2002, **202**, 269-279.

22. P. V. Kamat and D. Meisel, *Current Opinion in Colloid & Interface Science*, 2002, **7**, 282-287.

23. S. Kim and W. Choi, *Journal of Physical Chemistry B*, 2002, **106**, 13311-13317.

24. F. B. Li and X. Z. Li, *Chemosphere*, 2002, **48**, 1103-1111.

25. S. X. Liu, Z. P. Qu, X. W. Han and C. L. Sun, *Catalysis Today*, 2004, **93-5**, 877-884.

26. V. P. Poroshkov and V. S. Gurin, *Surface Science*, 1995, **331**, 1520-1525.

27. V. Subramanian, E. Wolf and P. V. Kamat, *Journal of Physical Chemistry B*, 2001, **105**, 11439-11446.

28. V. Subramanian, E. E. Wolf and P. V. Kamat, *Journal of Physical Chemistry B*, 2003, **107**, 7479-7485.

29. V. Subramanian, E. E. Wolf and P. V. Kamat, *Journal of the American Chemical Society*, 2004, **126**, 4943-4950.

30. I. H. Tseng, W. C. Chang and J. C. S. Wu, *Applied Catalysis B-Environmental*, 2002, **37**, 37-48.

31. I. H. Tseng, J. C. S. Wu and H. Y. Chou, *Journal of Catalysis*, 2004, **221**, 432-440.

32. M. Ni, M. K. Leung, D. Y. Leung and K. Sumathy, *Renewable and Sustainable Energy Reviews*, 2007, **11**, 401-425.

33. M. Bowker, P. R. Davies and L. S. Al-Mazroai, *Catalysis Letters*, 2009, **128**, 253-255.

34. V. M. Daskalaki and D. I. Kondarides, *Catalysis Today*, 2009, **144**, 75-80.

35. N. Luo, Z. Jiang, H. Shi, F. Cao, T. Xiao and P. P. Edwards, *international journal of hydrogen energy*, 2009, **34**, 125-129.

36. T. Kawai and T. Sakata, 1980.

37. T. Kida, G. Guan, N. Yamada, T. Ma, K. Kimura and A. Yoshida, *International journal of hydrogen energy*, 2004, **29**, 269-274.

38. I. Langmuir, *Journal of the American Chemical Society*, 1912, **34**, 1310-1325.

39. I. Langmuir, *Journal of the American Chemical Society*, 1916, **38**, 1145-1156.

40. H. S. Taylor and A. T. Williamson, *Journal of the American Chemical Society*, 1931, **53**, 2168-2180.

41. J. Lennard-Jones, *Transactions of the Faraday Society*, 1932, **28**, 333-359.

42. G. Binnig, H. Rohrer, C. Gerber and E. Weibel, *Surface Science Letters*, 1983, **131**, L379-L384.

43.   G. Binnig and H. Rohrer, *Ibm Journal of Research and Development*, 1986, **30**, 355-369.

44.   H. Conrad, G. Ertl and E. Latta, *Surface Science*, 1974, **41**, 435-446.

45.   G. K. Binnig, *Physica Scripta*, 1987, **T19A**, 53-54.

46.   M. Ramamoorthy, D. Vanderbilt and R. King-Smith, *Physical Review B*, 1994, **49**, 16721.

47.   U. Diebold, *Surface science reports*, 2003, **48**, 53-229.

48.   S. Nagarajan, K. Thirunavukkarasu and C. S. Gopinath, *The Journal of Physical Chemistry C*, 2009, **113**, 7385-7397.

49.   U. Burghaus, I. Jones and M. Bowker, *Surface science*, 2000, **454**, 326-330.

50.   I. Z. Jones, R. A. Bennett and M. Bowker, *Surface science*, 1999, **439**, 235-248.

51.   S. Nagarajan, K. Thirunavukkarasu, C. S. Gopinath, J. Counsell, L. Gilbert and M. Bowker, *The Journal of Physical Chemistry C*, 2009, **113**, 9814-9819.

52.   Y. Ma and T. Matsushima, *Catalysis today*, 2006, **117**, 90-97.

53.   R. Sharpe and M. Bowker, *Surface science*, 1996, **360**, 21-30.

Chapter 2 – Experimental

Contents

2   Introduction

The course of this research was divided into two parts; one part focussing on the surface science involved with the photocatalytic production of hydrogen, with the hope of gaining an understanding of the mechanism and kinetics, using an ultra high vacuum system, with molecular beam and XPS. The other aspect of the project will concentrate on making new powdered catalysts and measuring their reactivity using a photo-reactor.

2.1   Photocatalysis Experimental

The preparation method of catalysts used for the powdered photocatalysis element of this study is described below, along with the experimental set up and details of how reactions were carried out.

2.1.1   Catalyst Preparation

2.1.1.1   Preparation of Pd/Pt TiO_2 Catalysts

The palladium/platinum was deposited onto titania using the incipient wetness impregnation technique. The majority of the catalysts were made using P25 TiO_2 (Degussa) as the photocatalytic support, however the reported rutile titania catalysts were made using titanium(IV) oxide, rutile, 99.8% (Sigma Aldrich), with the exception being the rutile TiO_2 prepared by the Keller method and the anatase TiO_2 supplied by Raimon Perea Marín.

Typically, the preparation procedure was as follows. The appropriate mass of metal salt, calculated using Eq^n 1 detailed below, (Pd source – $PdCl_2$ and Pt source - $H_2PtCl_6.6H_2O$) was dissolved in acidified water to give the desired metal concentration; the solution was added dropwise to the TiO_2 support and ground using a pestle and mortar. The impregnated support was dried in an oven set to 120 ^{o}C for 2 hours and calcined at 500 ^{o}C for a further 3 hours. After calcination the catalyst was ground again in a pestle and mortar and passed through a 53 μm sieve.

For the preparation of 2 g 0.5 wt % of Pd on TiO_2, the amount of $PdCl_2$ needed was determined as follows below in equation 2.1;

$$mass\ of\ PdCl_2 = \frac{0.5}{100}\ \acute{}\ 2g\ \acute{}\ \frac{177.33\ g\ /\ mol\ PdCl_2}{106.42\ g\ /\ mol\ Pd} \qquad \mathbf{Eq^n\ 2.1}$$

$$= 0.0166\ g\ PdCl_2$$

2.1.1.2   *Ball Milling of the Rutile Titania Support*

The ball mill used was partially filled with the rutile titania and 80 1cm diameter ceramic balls and mechanically rotated at 50 rpm for 6 hours. Samples of the titania were removed from the ball mill every hour to generate a table of results on the effect of the different amounts of grinding experienced by the sample in the ball mill.

2.1.1.3   *Preparation of High Surface Area Rutile Titania*

The high surface area rutile was prepared by a sol gel procedure used by the Keller group[1]. An aqueous solution of hydrochloric acid (25 ml, 2 $molL^{-1}$) was added to titanium isopropoxide (15 mL) under vigorous stirring. The hydrosol was left to age at room temperature for 48 hours, before polyethylenglycol (PEG, 2 g) was introduced under stirring and the resulting mixture was dried at room temperature and further at 110 ^{o}C for 24 hours before calcination in air at 350 ^{o}C for 2 hours. The resulting titania support was loaded with Pd via the incipient wetness method described above. The morphology of the titania prepared by the sol gel procedure detailed above was confirmed using XRD, where the characteristic diffraction pattern for rutile titania was observed.

2.1.1.4   *Preparation of Anatase TiO₂ by the Supercritical Antisolvent Process*

The titanium precursor ($TiO(acac)_2$ or Ti-isopropoxide, 30 mg ml^{-1}) was dissolved in a solvent mixture of 2 % vol. $H_2O/MeOH$ (100 ml) and acetic acid (1 g). A flow of CO_2 (12 L

min^{-1} STP) and the solution (0.5 ml min^{-1}) were pumped into a rig stabilized at a pressure of 120 bar and a temperature of 40 ^{o}C. After 1 hour of precipitation, CO_2 was flushed through the rig to carry off the solvent trapped inside the precipitate. Finally the rig was depressurized to ambient pressure and the support precursor was collected and further calcined under static conditions at 450 ^{o}C for 5 hours (5 ^{o}C min-1)[2, 3]. The resulting titania support was loaded with Pt via the incipient wetness method described above.

2.1.2   Photoreactor Setup

Figure 2.1, below shows the photoreactor[4]: the pyrex glassware displayed on the left was used as the reactor, where the water, methanol and catalyst were contained during experiments and is detailed more thoroughly below, and the xenon lamp directly to the right of the glassware was the source of the "sun" in our reactions. The gas chromatograph shown in Figure 2.1 was used to measure the amount of hydrogen produced. The photoreactor is housed in a black box to protect us from the UV radiation produced by the xenon lamp and reduce any error from the changing light intensity from the laboratory window.
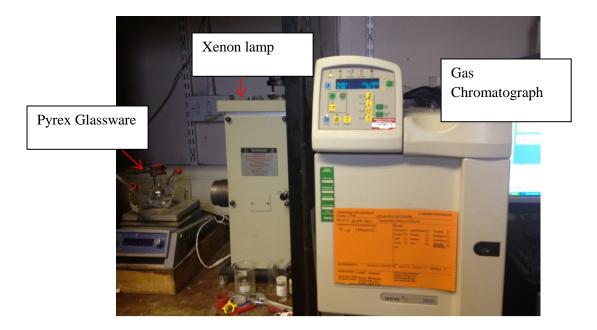

Figure 2.1: Photograph of photoreactor setup

2.1.2.1   Pyrex Reactor

Figure 2.2, below, shows the pyrex reactor for the photocatalysis experiment in more detail. The glassware has been specially designed to accommodate three "necks", two for purging the vessel with argon, i.e. an Ar inlet and an Ar outlet and the larger, vertical neck, to take gas samples from during reaction through a rubber septum and to provide space for the glass slides that hold the catalyst sample in the gas phase reactions. The 165 ml flask is made out of 2 mm thick pyrex material, to minimize light absorption and due to pyrex's ability to facilitate 92 % UV-visible light transmission through its walls[5]. The pyrex flask was situated above a hotplate, though no external heating was applied, reactions were carried out at room temperature, the presence of the hotplate was to enable stirring of the reaction solution during experimental allowing equal distribution of catalyst and reactants.
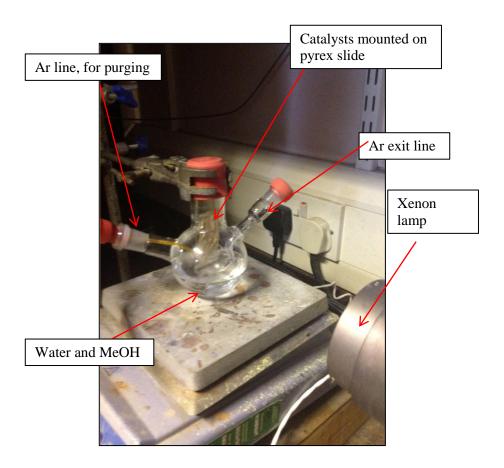

Figure 2.2: Pyrex reactor set-up for gas phase reactions.

The reactor has been arranged for a gas phase reaction in this image. The catalyst was mounted on a pyrex slide by adding a few drops of water to 0.2 g of the catalyst and applying this slurry using a spatula to the deep scratches etched on the pyrex slide before leaving overnight for the water to evaporate. The dried catalyst mounted on the pyrex slide was positioned 2 cm above the methanol/water solution, so none of the catalyst actually comes into contact with either of these compounds in their liquid form. For the gas phase reactions the liquid solution was made up of 50 ml water and 100 µL of MeOH (Sigma Aldrich 99.8%) unless otherwise stated.

In a liquid phase reaction 0.2 g of the catalyst would be placed in a solution made up of 100 ml of water and 100 µL of MeOH (Sigma Aldrich 99.8%) unless otherwise stated.

For both gas and liquid phase reactions, the liquid solution and gaseous chamber of the flask was purged for 30 minutes before MeOH was added, the reaction vessel was sealed off and the light source was introduced. 0.2 ml samples of gas were taken at 30 minute intervals for three hours. Experiments were repeated to account for experimental errors.

Figure 2.3 details the optical arrangement for the gas and liquid phase reactions, the light trace diagram also provides perspective of the un-collimated light source used during the reactions.
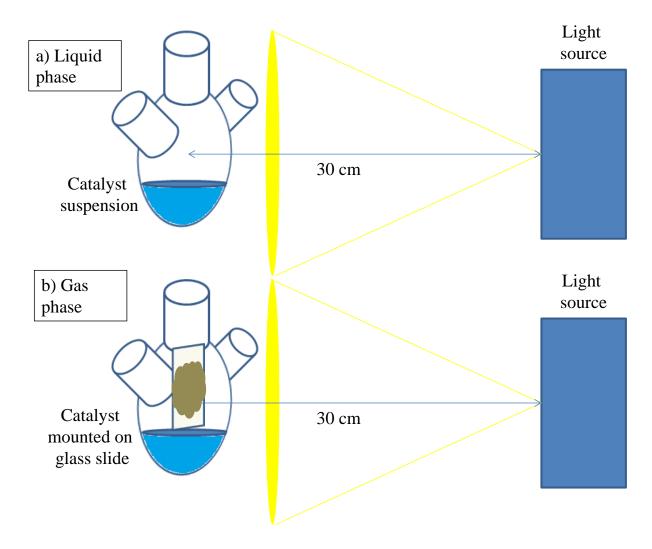
Figure 2.3: Light trace diagram demonstrating the optical arrangement for the gas and liquid phase experiments.

2.1.2.2   Light Source

A 400 W xenon arc lamp, Oriel model n° 66084, was used as the light source in our experiments and can be seen in both Figure 2.1 and Figure 2.2. The range of light produced by this lamp from 200 nm – 1100 nm covers parts of the UV, visible and infrared spectrum, with an intense UV region suitable for this study, note, pyrex glass cuts off all wavelengths below 300 nm. The lamp was situated directly in front of the reactor vessel, so that the emitted light would enter the flask through the side of the flask, the lamp, ignitor, condensing optics, rear reflector and lamp cooling fan were all held within an arc lamp housing, Oriel model n° 66921 and connected to an external power supply (Newport model n° 69920).

Previous studies in the Bowker group using the method set out by Pitts[6] calculated the output for the Oriel lamp used in these phototcatalysis studies to have the photon flux with respect to wavelength shown in Table 2.1 below. These incident photon fluxes have not been used in this study to calculate the quantum yield of the photocatalytic methanol reforming reaction under investigation, consequently all hydrogen production values stated in the results chapters have not been photon-normalised.

Region, nm	Number of Photon, Einstein $L^{-1}s^{-1}$
350 – 410	1.03×10^{-7}
280 – 400	6.96×10^{-7}
260 - 320	6.24×10^{-8}

Table 2.1: List of photon flux wrt wavelengt determined using 2-nitobenzaldehyde actinometry.

2.1.2.3   Gas Chromotography (GC)

The 0.2 ml gas samples taken periodically during these experiments using a gas tight syringe (from SGE) were injected into a gas chromatogram to gain quantitative and qualitative information on the gases present and evolved during the photocatalytic reaction. The distinction between the different gases present derives from their different elution times to travel through the column housed in the GC oven. The differing elution times arise from the gaseous compounds present in the sample having different affinities to the stationary phase of the column, irrespective of the constant flow of carrier gas, in this case argon due to its contrasting thermal conductivity to hydrogen, hence improving the TCD sensitivity towards H_2. Once the sample has negotiated its way through the GC column it passes over a thermal conductivity detector filament, which relays the thermal conductivity of the gases to give qualitative and quantitative data on the gases present. A Varian 3300 gas chromatograph equipped with a thermal conductivity detector (TCD) and a 2 m long MS 13X column was used in this study, with the following set up conditions; a carrier gas flow rate of 30 ml / min,

both the injector port and column temperature were set at 50 ^{o}C and the detector was set at 120 ^{o}C.

2.1.2.4   Hydrogen Calibration

An example of a gas chromatograph produced from these experiments is shown in Figure 2.3, since these data are difficult to interpret we need to convert them to more workable plots showing hydrogen volume evolved rather than GC peak areas with units of uV/min, this can be done using a simple calibration curve.
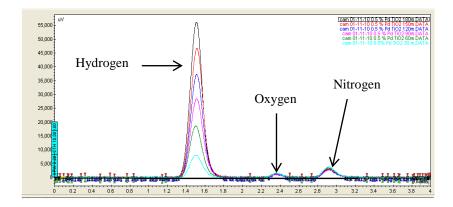
Figure 2.4: GC data for 0.5 wt% Pd/TiO2 in liquid phase methanol reforming photoreaction.

To generate a calibration curve, a plot of volume versus peak area was produced, see Figure 2.4 below, by injecting known volumes of high purity hydrogen (99.998 % BOC gases) into the GC and recording the corresponding area of the hydrogen peak; the gradient of this graph could then be used to convert unknown areas from chromatographs into a volume of hydrogen.
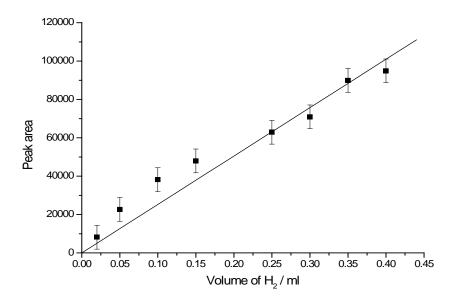
Figure 2.5: Hydrogen calibration plot.

This volume could then be scaled up to represent the gaseous volume present in the reaction vessel during the reaction, which is known to be 65 ml for liquid phase reactions and 115 ml for gas phase reactions, using the equation below, Eq^n 2.2:

$$\textit{Volume of } H_2 \textit{ in the syringe, ml} = \frac{\textit{Peak area}}{\textit{Calibration}\_\textit{gradient}} \qquad \textbf{Eq}^n\textbf{ 2.2}$$

$$\textit{Volume of } H_2 \textit{ in the flask, ml} = \frac{\textit{Volume of the } H_2 \textit{ in syringe}\acute{}\textit{ gas volume of the flask}}{\textit{gas volume in the syringe}}$$

2.1.3   Catalyst Characterisation

Surface areas, where stated were, determined using BET (Brunauer, Emmet and Teller) machine. X-ray diffraction (XRD) was used to confirm the crystalline state of the titania catalysts as either, anatase, rutile or mixture as observed in P25 TiO_2.

2.2   Ultra High Vacuum Experimental

For the surface science aspect of this research project a combination of x-ray photoelectron spectroscopy and molecular beam was used to investigate the behaviour of the surface of model catalysts used in the photocatalytic reactions to try and understand the mechanism and reaction properties.

Ultra high vacuum (UHV) conditions, typically between 1 x 10^{-8} millibar (mbar) and 1 x 10^{10} mbar, were essential for these surface sensitive techniques to be successful, since any compounds present in the background pressure can adsorb and rapidly contaminate the surface.

Detailed below are the methods used to achieve UHV conditions and explanations of how the surface sensitive techniques enrolled in this study work.

2.2.1   Analysis Chamber

The molecular beam system used in this study comprises a stainless steel UHV chamber maintaining a base pressure of ~1 x 10^{-10} mbar which increased to ~1 x 10^{-9} mbar during the course of the adsorption experiments. The diagram in Figure 2.5 below shows a schematic view of the interior of the analysis chamber, detailing the position of the x-ray gun, mass spectrometer and molecular beam in relation to the manipulator, which houses the model catalyst under investigation. The sputter gun is not visible in either Figure 2.5 or Figure 2.6 since it is located directly below the x-ray gun at an angle of 45 $^{\circ}$. The analysis techniques present in the chamber will be discussed in more detail later in this chapter.

Evacuating the main chamber to achieve and maintain UHV was made possible using several pumps and heating to drive gas molecules from the interior walls and was carried out as follows. Once the chamber was fully sealed, a rotary pump was utilised to initially reduce the pressure from ambient to ~2 x 10^{-2} mbar, by drawing gas in from the system and compressing it before expelling it through a spring loaded exhaust valve. Before 'bake-out' could begin the pressure was reduced further to ~1 x 10 $^{-7}$ mbar, by the introduction of a Leybold TurboVac 600C turbo molecular pump (N_2 pumping speed of 560 Ls^{-1}), which was situated

at the base of the analysis chamber. The turbo molecular pump reduces the pressure by physically removing molecules upon collision with the series of blades and discs fitted to the rotor that rotates at the same order of magnitude as the velocity of gas molecules moving in the main chamber[7]. Upon extraction from the main chamber the gases removed are expelled to the atmosphere through a backing pump.
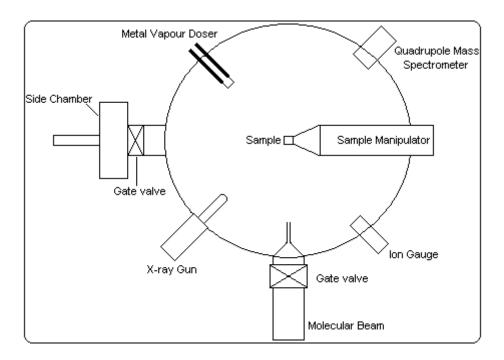

Figure 2.6: Diagram to show top down view of interior of UHV chamber.

To reduce the pressure in the main chamber further and reach UHV conditions the system needed to be heated to a high enough temperature (140 ^{o}C) to desorb contaminants such as water, carbon monoxide and carbon dioxide from the inside walls of the stainless steel chamber and apparatus contained within. The temperature was achieved through a combination of ceramic heaters and heating tapes, while the chamber was covered with a large fiberglass tent, to insulate the system. The bake-out could take up to 48 hours to complete. The filaments of apparatus housed in the analysis chamber were degassed whilst the chamber was still warm to desorb any contaminants adsorbed over the bake-out period, by inducing thermal desorption of these gaseous molecules through gradually increasing the current passing through each filament up to their operating current. Upon completion the base pressure in the analysis chamber was 1 x 10^{-10} mbar. The analysis chamber was equipped

with a thermal conductivity gauge and a thermionic ionisation gauge, respectively, to monitor the reduction in pressure from atmosphere to UHV, firstly, a Pirani gauge was used to monitor the ambient pressures between 1 bar and 1×10^{-3} mbar, and a Bayard-Alpert (BA) gauge was needed to record lower pressures from 1×10^{-3} mbar to 1×10^{-11} mbar.
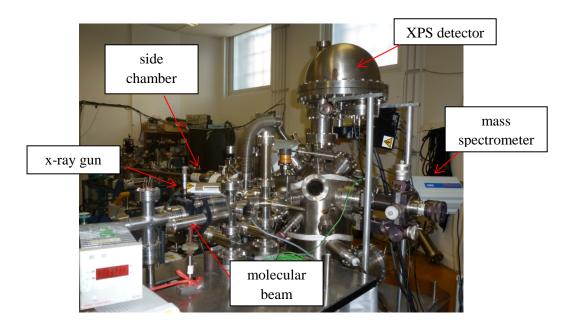

Figure 2.7: Photograph of XPS/molecular beam system.

UHV conditions are essential to provide atomically clean surfaces for surface analysis. Since contamination of a surface is directly related to the rate at which gaseous molecules collide with the surface, the effect reducing the background pressure has on the time taken to contaminate a surface can be calculated using the Hertz-Knudsen equation:

$$Z = \frac{p}{(2\pi m kT)^{1/2}}$$

Eq^n 2.3

Equation 2.3. p = ambient pressure (Ncm^{-2}), m = molecular mass (kg molecule^{-1}), k = Boltzmann constant (J K^{-1}) and T = temperature (K).

The rate of surface contamination is also dependent upon the sticking probability (S) of the molecule concerned on the surface being investigated. Sticking probability can be expressed as follows in equation 2.4:

$$S = \frac{\text{Rate of adsorption of molecules by the surface}}{\text{Rate of collision of molecules with the surface}} \qquad \textbf{Eq}^{\textbf{n}}\textbf{ 2.4}$$

For S = 1, a monolayer coverage of adsorbate has been formed on the surface and saturated every surface site. Carbon monoxide, a typical gaseous contaminant, readily adsorbs onto the surface of several metals. Using the Hertz-Knudsen equation (equation 2.3), it is possible to calculate the rate of surface contamination of CO at 298 K and background vacuum pressures of 1×10^{-6} mbar and 1×10^{-10} mbar respectively (where 1 mbar = 1×10^{-2} Ncm^{-2}).

$$Z = \frac{(1 \times 10^{-2} \times 10^{-6})}{[2 \times \pi k \, (\frac{28}{1000 \times 6.02 \times 10^{23}}) \times (1.38 \times 10^{-23}) \times 298]^{1/2}}$$

$$Z = 2.885 \times 10^{14} \text{ cm}^{-2} \text{ s}^{-1}$$

Assuming the surface consists of approximately 1×10^{15} atoms cm^{-2} (typical of most surfaces), then the rate of contamination of that surface by CO at a pressure of 1×10^{-6} mbar would be:

$$\frac{2.885 \times 10^{14} \text{ cm}^{-2} \text{ s}^{-1}}{1 \times 10^{15} \text{ cm}^{-2} \text{ per monolayer}} = 0.2885 \text{ monolayers s}^{-1}$$

Therefore it would only take 3.5 seconds to adsorb one monolayer of CO at 298 K and 1×10^{-6} mbar background gas pressure. If the same surface hypothesised above was exposed to the same background gas at a pressure of 1×10^{-10} mbar, saturation with a monolayer of CO would consequently take over 9 hours, providing adequate time to carry out any surface analysis.

2.2.2   Sample and Reactant Preparation

Two metal crystals were used in this study to represent the model catalyst under investigation. A Pd(110) (Metal and Oxides, 5N purity) single crystal and a TiO_2 (110) single crystal.

The Pd (110) had grooves along the edge of the crystal allowing it to be mounted directly onto the sample manipulator via two tungsten wires (0.125 mm diameter, 99.95% purity, Advent Research Material Ltd). However, the absence of a similar set of grooves on the TiO_2 (110) single crystal, meant that the crystal had to be initially mounted onto tantalum foil to create a vessel to hold the sample in and attach it via two tungsten wires to the manipulator. For both the Pd and the TiO_2 samples the tungsten wires were also used to resistively heat the sample. The temperature of the samples was measured using a chromel-alumel thermocouple, which in the case of the Pd (110) crystal was inserted into a small hole, drilled in the side of the crystal and for the TiO_2 crystal was inserted into a hole in the back of the Ta foil holder, so as to touch the back of the crystal.

Carbon was the main surface impurity present on the Pd(110) surface and was removed via a series of sputter-anneal cycles described as follows, flashing the sample to 1173 K, sputtering with 0.5 kV Ar^+ at 673 K, flashing to 1173 K again, annealing the sample in oxygen at 773 K, before flashing to 1173 K once more. The absence of a C 1s peak (284 eV) on an XP spectrum was used as an indication of the surface cleanliness.

The TiO_2(110) was cleaned by flashing to 673 K, sputtering with 0.5 kV Ar^+ at 298 K, before annealing the sample in oxygen at 673 K. This proved sufficient enough to remove surface impurities and also replace any lost bridging oxygen's removed during the sputtering procedure. XPS was utilised to confirm that the Ti 2p peaks (455 and 461 eV) were in the correct place and fully oxidised to Ti^{4+} character.

Argon and oxygen were used from lecture bottles provided by Argo Ltd, with purities of 99.999 % and 99.6 % respectively. All lecture bottles were fitted to the main gas line of the molecular beam system. The pressures of the gases in the molecular beam were monitored via an electronic pressure gauge. A series of taps and valves were utilised accordingly to direct the required gas to the molecular beam, sputter gun and the leak valve to the main UHV chamber. Crotonaldehyde (predominantly *trans,* ≥99%, containing 0.1-0.2% BHT as

stabilizer, 1% H_2O as stabilizer) was fitted to the main gas line of the molecular beam in a glass tube and freeze thawed prior to beam experiments.

2.2.3   Quadruple Mass Spectroscopy

Mass spectroscopy was employed in this study to identify the residual gas composition of the main chamber, to monitor the purity of the gases used, for leak checking and for recording molecular beam experiments. The ThermoVG QMS (quadrupole mass spectrometer) housed in the analysis chamber was well suited to these applications due to its ability to accurately record several masses for extended periods of time. This was of particular importance during molecular beam experiments, allowing the reactivity of the incident beam and product evolution to be measured simultaneously.
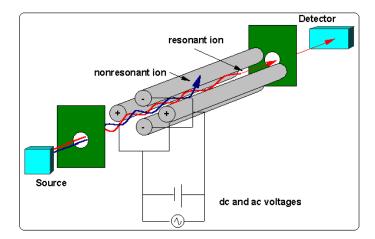

Figure 2.8: Schematic diagram of a quadrupole analyser.

The QMS follows the same procedures as all mass spectrometers, something to ionise the molecules into a beam of particles, something to then separate these ions and finally something to measure the mass-to-charge ratio (*m/z*) of these ions. The quadruple analyser is the component of the spectrometer that separates the ions before they reach the detector, permitting the user to only record masses of interest. Figure 2.7, is a simplified representation of the quadrupole analyser and shows two pairs of parallel rods, each pair is electrically connected, by the application of a direct-current (dc) and an alternating current potential

between either pair giving rise to an oscillating electric field, which enables mass separation. As ions travel down the quadrupole, a defined set of dc and ac potentials accommodate the passage of ions with a particular mass-to-charge ratio (resonant ions), whilst all other ions (non-resonant ions) will become unstable and stray from their original trajectory, eventually colliding with the rods. A spectrum is obtained by detection of the ions passing through the quadrupole filter as the voltages of the rods are varied and allows the selection of ions with a particular *m/z*.

2.2.4 Molecular Beam

A "molecular beam" is a narrow, well-defined source of gaseous atoms or molecules incident to a crystal sample surface, that can be used to identify the microscopic features of surface reactions in an attempt to determine how these reactions occur at a particular surface[8, 9]. In this study a molecular beam was used to investigate surface-adsorbate structure and reactivity for several molecules on the surface of a Pd (110) crystal. The combination of a skimmer and a collimator placed in series along the path of the molecular beam backscatters many of the incoming molecules and transforms the remaining gas molecules into the highly defined beam experienced at the surface of the material under investigation. Figure 2.8[10] below illustrates the thermal nozzle source molecular beam employed in this research and a schematic detailing the backscattering that occurs during the collimation process.

A series of differential pumping stages are present along the beam line, to maintain UHV when the molecular beam enters the main chamber, and are displayed in Figure 2.8 below. The beam line described is made up of a four way cross junction connecting the gas line to the beam line and backed by a Leybold rotary vane pump, followed by two six way cross junctions. The six way cross junction act as a beam production chamber and a beam defining section, respectively, with the latter containing a 'beam flag' that prevented the full flow of the molecular beam from entering the main UHV chamber until it was required. Each six way junction was backed by a Leybold TurboVac 50 turbo molecular pump (N_2 pumping speed 1 x 10^{-3} mbar of 55 Ls^{-1}), in turn backed by a Leybold rotary vane pump. A fast acting gate valve, divided the molecular beam from the UHV chamber, allowing the beam line to be fully isolated from the main UHV chamber when necessary. Finally, a "chamber flag" located within the main analysis chamber was utilised during beam experiments to interrupt the gas

beam hitting the surface of the sample at will, which when open allowed the delivery of a 2.9 mm diameter beam of molecules at the sample with a flux of 1.5×10^{17} molecules $m^{-2}s^{-1}$, the physical sizes of the quartz capillary, the conical skimmer and the Pyrex tube are described in detail by Bowker et al[11].
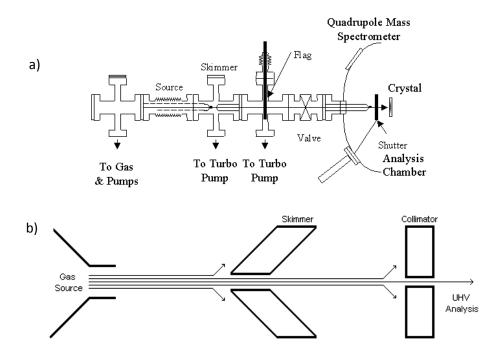

Figure 2.9: Schematic diagram of the experimental set-up for a molecular beam. a) Illustrates the molecular beam used in this research. b) Indicates the collimation process that is used to define the molecular beam via the backscattering of many incoming molecules from the gas line.

The high flux of molecules from a molecular beam makes any intermolecular collisions insignificant, hence, ensuring that molecules arriving at the sample surface from the beam line are intact and any products detected by the QMS are a direct result of a surface reaction occurring between the incident beam and the sample surface. Sticking probabilities and surface coverages can be calculated from molecular beam data, which when combined with the observed reaction products observed through QMS can provide insights into the mechanism of the reaction under investigation.

An even flux across the sample was essential to guarantee that any data retrieved from molecular beam experiments were representable. Optimal flux was achieved by aligning the beam in order to minimise the penumbra experienced at the sample surface. Figure 2.9,

shows the umbra and penumbra distances for two different beams, where Beam 1's constant flux, or umbra, region would be a couple of millimetres wider on the sample surface than for Beam 2, ensuring a relatively large surface area of constant flux for sticking measurements.
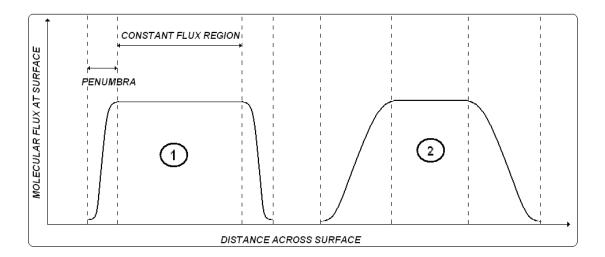

Figure 2.10: Umbra and penumbra distances vs. flux for two different beams.

Upon achieving optimal conditions for surface reactions, as described above, molecular beam reactions were carried out using the method outlined by Kings and Wells[12, 13]. Fundamentally this process involves monitoring the change in chamber pressure, which occurs during disruption of the molecular beam, as a direct result of the surface characteristics under investigation, this process and calculation will be discussed in detail below.

2.2.4.1   Sticking Probability Calculations

Sticking probability calculations were measured through monitoring the partial pressure changes recorded by mass spectrometry during a molecular beam profile experiment. Figure 2.10 describes the gate and flag opening/closing stages involved during a molecular beam experiment of CO adsorption on a clean Pd (111) single crystal at 333 K. At point 1 the multiple ion monitoring program has been set to record, as described above at point 2 the shutter on the molecular beam has been opened to allow the beam of CO molecules to enter the chamber. Point 3 is the point at which the Pd (111) single crystal is incident to the CO molecular beam. Points 4 and 5 are the reverse steps performed at points 3 and 2 respectively.
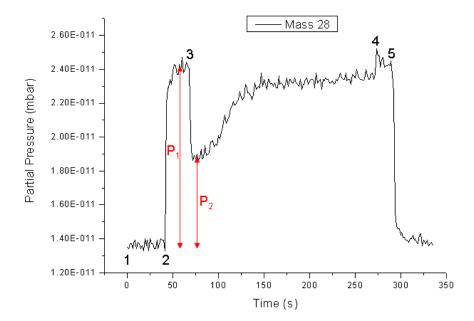
Figure 2.11: Typical beam profile for CO adsorption on a clean Pd(111) single crystal at 333 K taken from L. Gilbert thesis, used to describe sticking profile calculations.

The initial sticking probability of CO on the Pd(111) surface at this particular temperature is related to the two pressures, P_1 and P_2, shown in Figure 2.10.

$$S_{(t)} = \frac{(P_1 - P_2)}{P_1}$$

Eqⁿ

2.5

The changes between P_1 and P_2 can be directly related to CO adsorption on the surface of the Pd(111) single crystal surface. When the beam flag is moved at point 3, the sample surface is effectively acting as a 'pump', adsorbing CO molecules onto its surface and removing them from the background chamber pressure. This is why the partial pressure of CO decreases when the sample is exposed to the molecular beam. After the relatively large initial sticking of CO, the surface begins to saturate, with the partial pressure of CO slowly returning to the level it was at point 3. Eventually, the sticking of an incident CO molecule becomes less and less probable until the surface is fully saturated. The sticking probability at any given time ($S_{(t)}$) can be calculated by using equation 2.5.

2.2.5 Metal Vapour Deposition

A model of the powdered catalysts used in the photocatalysis part of this study was fashioned for surface analysis by depositing palladium onto the surface of the $TiO_2(110)$ single crystal. Metal vapour deposition was achieved using an in-house constructed Pd evaporator as illustrated in Figure 2.11.
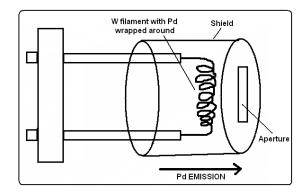

Figure 2.12: Schematic of the Pd evaporator used for metal vapour deposition.

The MVD equipment was made up of a tungsten/palladium wire attached to two threaded steel rods via two nuts and encased in a shield with a small aperture at one end. The W/Pd wire was made by tightly coiling Pd wire (0.1 mm diameter. 99.97% purity, Alfa Aesar) around W wire (0.15 mm diameter, 99.95% purity, Advent Research Materials Ltd), and coiled approximately ten times to create the filament of the depositor. A beam of vaporised Pd was generated by applying a current through the W/Pd filament, while the length of time the $TiO_2(110)$ surface was exposed to the Pd beam dictated the amount of metal coverage the surface experienced. A 'shield' was employed to retain energy by reflecting heat back to the filament and to minimise the amount of evaporated Pd deposited onto the interior walls of the UHV chamber and instruments contained within. The deposition of palladium onto the catalyst support was followed using the surface sensitive analytical technique known as x-ray photoelectron spectroscopy and is described below, section 2.2.6.

2.2.6 X-ray Photoelectron Spectroscopy

Analysis of the two crystal surfaces under investigation in this study were conducted using the powerful analytical technique called x-ray photoelectron spectroscopy, often abbreviated to XPS. The technique was developed by Kai Siegbahn[14] to practically utilize the photoelectric effect discovered by Hertz[15] and explained by Einstein[16].

The basis of XPS focuses on the light-matter interaction whereby photoelectrons (light) can induce electron (matter) emission from a solid. For this phenomenon to occur the energy of the incident photons must be greater than the energy required to expel an electron from its parent atom to a sufficient distance outside the solid surface that it no longer feels the positive attraction of the hole created as a result of its removal (ie from the highest occupied level to the 'vacuum level'), this is known as the workfunction, ϕ, of a solid.

The source of the photons used to excite photoemission in the analytical technique described here is a monochromatic beam of x-rays. The energetic source causes electrons from both core and valence shells of a solid to be emitted, and is shown in Figure 2.12 below. Since core electrons originate from the inner quantum shells of a solid, where the influence of the atomic nucleus is paramount in the condensed phase, these electrons retain the atomic characteristic binding energies (E_B) associated with the solid.
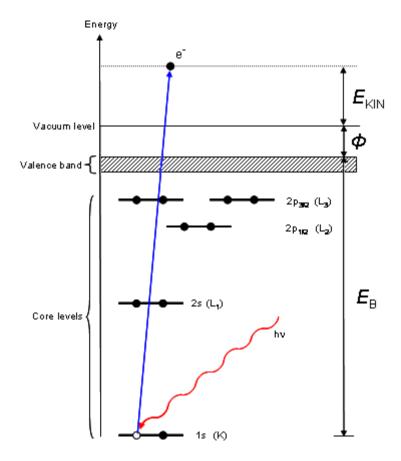
Figure 2.13: Principles behind the excitation of a core level electron.

Through the application of energy conservation, ie the incident photon of energy (hυ) can only give up all or none of its energy, then E_B can be calculated by measuring the kinetic energy of the core level electron emitted by the XP source, using Eq^n 2.6 and the atomic resolution of the surface can be deduced.

$$\text{K.E.} = h\upsilon - E_{B+}\ \phi \qquad\qquad \textbf{Eq}^n\ \textbf{2.6}$$

Since the photon energy, hυ, is known and photoemission from an atom with well-defined core levels will produce electrons with well-defined kinetic energies varying from element to element, equation, Eq^n 2.6 can be used to calculate the binding energy. It follows that the higher the atomic mass of an atom the higher the nuclear charge of its nucleus and the higher the binding energy of a given core level. The oxidation state of an element at the surface can also be identified by considering how the binding energy of an emitted electron will depend on the species to which it is bonded. Consider TiO_2, where Ti is present in its +IV oxidation

state , electrons in the core level experience higher columbic effect and as an effect a higher binding energy than core level electrons in a lower oxidation state Ti atom, electrons emitted from a high oxidation state will have a lower kinetic energy, this phenomenon is known as the chemical shift. Commonly XP spectra output the KE measured as E_B to ease elemental identification.

The incident x-ray generated photons have enough energy to travel millimetres into a solid, which for the crystals under investigation here means that the incident photons could travel through the solid. The behaviour of the emitted electrons is what makes this technique surface sensitive, particularly their inelastic mean free path, IMFP. The IMFP for an electron gives a guide to how far it can travel through a solid before losing energy, specifically the distance before it is inelastically scattered and its intensity decays to 1/e of its initial value, this distance can be calculated using Eq[n] 2.7 below. It follows that any electrons emitted from the bulk of the crystal will not have enough energy to escape from the solid, hence any electrons detected at the XPS sensors must be emitted from surface atoms.

$$I(d) = I_0 \exp\left(\frac{-d}{\lambda(E)}\right)$$

Eq[n] 2.7

Upon emission of a core level electron from a surface there will be an electron 'hole' left behind, this vacancy can either be filled by an electron in a higher energy level occupying the 'hole' and the difference in its energy state being released as a photon (x-ray fluorescence) or the energy difference can be transferred to a higher energy electron, which in turn is emitted to the vacuum level (auger electron) and detected and output in the XP spectrum. Auger electron emission is seen at high binding energies and can be utilised in addition to XP electron emission in XP spectra to analyse a surface but for this study have not been exercised.

Another feature of XP spectra that is familiar to other spectroscopic techniques is the occurrence of spin-orbit coupling, for orbitals with angular momentum >= 1. These doublets are present for p,d and f orbitals with the higher orbital momentum state appearing at higher kinetic energies (lower binding energy).

By only allowing electrons of a given kinetic energy, (the "pass energy"), to reach through to the detector results in the observation of continuous spectra. The pass energy is obtained using a combination of slowing electrons down initially to the pass energy, using a retarding

plate and removing any additional electrons that are still too fast or slow using a concentric hemispherical analyser (CHA), detailed below in Figure 2.13 The momentum of fast electrons is too great for their path to be changed enough for them to get around the hemispherical pathway whereas electrons which are too slow do not have enough momentum and so are pulled into the walls by the electric field. By varying the negative voltage on the retard plate the pass energy can encompass a range of kinetic energies, allowing a spectrum of differing KEs through to the analyser.
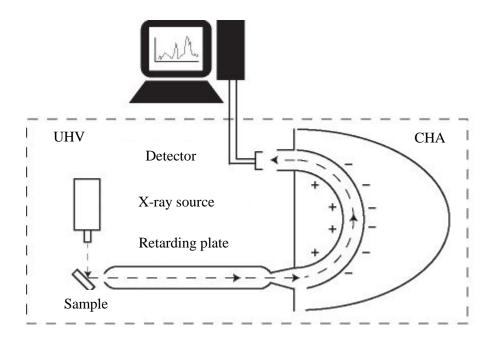

Figure 2.14: Schematic of concentric hemispherical analyser used in XPS.

The XPS analyser employed during this study, comprised a TX400/2 model x-ray gun from PSP vacuum technology, which consisted of a twin anode source that is capable of producing both magnesium Kα (1253.6 eV) and aluminium Kα (1486.6 eV) excitation energies for XPS. A thin Al window was positioned between the source and the sample to filter out the k –β radiation as well as preventing stray electrons and heating effects to impact the surface during analysis.

Output spectra were analysed using Casa XPS software and used to identify surface composition, which was crucial during metal vapour deposition of palladium on the titania single crystal and will be discussed in detail in chapter four.

2.3   References

1.   F. Bosc, A. Ayral, N. Keller and V. Keller, *Applied Catalysis B-Environmental*, 2007, **69**, 133-137.

2.   G. J. Hutchings, J. A. Lopez-Sanchez, J. K. Bartley, J. M. Webster, A. Burrows, C. J. Kiely, A. F. Carley, C. Rhodes, M. Havecker, A. Knop-Gericke, R. W. Mayer, R. Schlogl, J. C. Volta and M. Poliakoff, *Journal of Catalysis*, 2002, **208**, 197-210.

3.   Z. R. Tang, J. K. Edwards, J. K. Bartley, S. H. Taylor, A. F. Carley, A. A. Herzing, C. J. Kiely and G. J. Hutchings, *Journal of Catalysis*, 2007, **249**, 208-219.

4.   A. J. Dickinson, University of Reading, 1997.

5.   CORNING, *Pyrex technical data*, www.quartz.com/pxprop.pdf.

6.   J. N. Pitts, J. M. Vernon and J. K. S. Wan, *Air and Water Pollution*, 1965, **9**, 595-600.

7.   A. F. Chambers, R. K.; Halliday, B. S. , *Basic Vacuum Technology*, Institute of Physics, 1998.

8.   M. Bowker, Q. Guo and R. W. Joyner, *Surface Science*, 1991, **257**, 33-40.

9.   B. Poelsema, S. T. Dezwart and G. Comsa, *Physical Review Letters*, 1982, **49**, 578-581.

10.   M. Bowker, *Applied Catalysis a-General*, 1997, **160**, 89-98.

11.   M. Bowker, P. D. A. Pudney and C. J. Barnes, *Journal of Vacuum Science & Technology a-Vacuum Surfaces and Films*, 1990, **8**, 816-820.

12.   P. Alnot, A. Cassuto and D. A. King, *Faraday Discussions*, 1989, **87**, 291-302.

13.   D. A. King and M. G. Wells, *Surface Science*, 1972, **29**, 454-&.

14.   K. Siegbahn, *Atomic, molecular and solid state structure studied by means of electron spectroscopy*, Almqvist & Wiksells, Uppsala, 1967.

15.   H. Hertz, *Annalen der Physik und Chemie* 1887, 973.

16.   A. Einstein, *Annalen Der Physik*, 1905, **17**, 132-148.

Chapter 3 - Photocatalytic Hydrogen Reforming

Contents

3   Introduction

As detailed in Chapter 1, hydrogen production via water splitting is an ideal sustainable fuel source, however it is worth reiterating the difficulty associated with direct water splitting, i.e. evolution of both oxygen and hydrogen simultaneously, due to the high energy requirements and fast recombination of products experienced. Indirect water splitting is therefore a more common source of research material, and focusses upon the separate extraction of either oxygen or hydrogen from the parent water molecule. This is mainly achieved by the use of sacrificial reductants or oxidants.

The research presented here will focus on producing hydrogen by methanol reforming, where methanol is used as the sacrificial agent in the photocatalysis mixture, rather than production of both oxygen and hydrogen via direct water splitting.

3.1   Hydrogen Production by Reforming of Sacrificial Organic Agents

The high Gibbs free energy required to initiate direct water splitting introduces the need for an indirect route to hydrogen production using light energy, since the first report[1] of "electrochemical photolysis of water" there have been thousands of publications, and hundreds of reviews in this area. The work presented here focuses on methanol reforming, which is one of many sacrificial agents that have been investigated for their ability to improve the hydrogen productivity despite being non-renewable reactants that are used up during the reaction course; some such reagents have been reviewed by Rossetti from Milan University[2].

The important features of using organic sacrificial agents in photocatalytic reforming to produce hydrogen are that they can be exploited under ambient conditions and require relatively low tech chemical methods to report successful yields, when compared directly to thermochemical processes such as steam reforming of methanol. Several studies have also been conducted into the use of products that can be derived from biomass for use as sacrificial agents in the photocatalytic reforming process, for example, ethanol, glycerol[3], glucose, sucrose[4, 5], starch and wood[6] and even sewage sludge[7]!

The sacrificial agents act as hole scavengers during photocatalysis and are more easily oxidised by photogenerated valence-band holes than water alone, the hydrogen ions generated as a result of this process are then able to undergo reduction at the cathodic site on the catalyst.

3.1.1   Previous Group Research

As discussed previously photocatalytic hydrogen evolution from water alone is proven to have low reaction rates[8] and the most substantial work by the group has been focussed on various reactant mixtures, markedly methanol/water systems[3, 9, 10], which give the overall reaction shown below (Eq[n] 3.2):

$$CH_3OH + H_2O \rightarrow 3H_2 + CO_2 \qquad \textbf{(Eq}^{\textbf{n}}\textbf{ 3.2)}$$

Titania (TiO_2) has been extensively used as a semiconductor for photosensitizing water splitting[11, 12] and has been the major metal support investigated within the Bowker group towards photocatalytic production of hydrogen[8, 13-16]. Titania alone has low catalytic activity but its activity is increased significantly if a metal is deposited on the surface. One of the main metals investigated with the titania support has been palladium[8, 13, 14, 16], with the optimum loading for hydrogen evolution found to be 0.5 %wt. Pd/TiO_2. Other promising metal particles were found to be gold, iridium and platinum, however with the exception of gold[15]; none of these metals were tested to any extent within the group but there is lots of literature relating to platinum[17, 18]. Transition metal complexes have also been studied by other groups[19, 20].
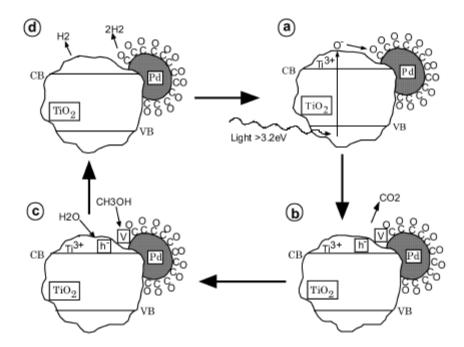
Figure 3.1: Diagram taken from Bowker at al[21], depicting the proposed mechanism of the photocatalytic reforming of methanol on Pd/TiO$_2$.
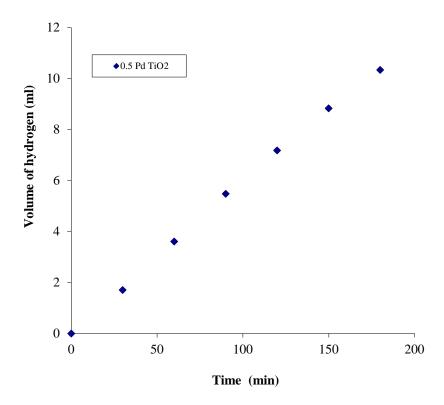
A catalytic cycle has been proposed for the photocatalytic reforming of methanol on Pd/TiO$_2$[9, 21] (see Figure 3.1). In this proposed mechanism light plays an essential role in enabling the steady state reaction to take place, by generating an activated oxidising species which removes surface CO from the supported Pd. The active centre for the reaction occurs at the interfacial sites between the support and the metal. Figure 3.1 shows how hydrogen is liberated when vacancies on the Pd particle are filled with methanol, leaving adsorbed carbon monoxide, which in the absence of light poisons the surface.

This project is aimed at improving our understanding of the above mechanism by combining studies of real catalysts with model systems to understand more about the fundamental kinetics, mechanisms and intermediates involved in these reactions which have great import for the future of mankind.

Particular emphasis has been paid to the design of the catalyst in this research, to improve our understanding of the mechanism involved during this process with the overall aim of improving the efficiency of hydrogen production. In addition, there is a small section investigating the production of hydrogen via reforming of other organic sacrificial agents.

3.2   Results and Discussion

3.2.1   Standard Pd/TiO$_2$ Catalyst

Figure 3.2: Photocatalytic hydrogen production from water/methanol mixture using a 0.5 %wt. Pd/TiO$_2$ catalyst

Figure 3.2 shows the volume of hydrogen produced over 3 hours by a 0.5 %wt. Pd/TiO$_2$ catalyst, after irradiation of the methanol solution with UV light as described in the experimental chapter. From previous work within the group the 0.5 wt% Pd/TiO$_2$ catalyst has been found to be the most successful palladium catalyst[21] and as a result is used as the basis for comparison for other photocatalytic reactions performed in the present research.

3.2.2   Loading Dependence: Variation between Gas and Liquid Phase

3.2.2.1   *Pt Loading Dependence: Variation between Gas and Liquid Phase*

Previous unpublished work within the group investigated the metal dependence of the catalyst in the methanol reforming reaction [22], which found that platinum had a similar rate in

the photocatalytic reaction. However unlike the palladium catalysts the weight loading of the platinum titania catalysts was never explored. Hence the metal loading dependence for several different platinum catalysts prepared via the incipient wetness precipitation technique were tested for their photocatalytic activity in the liquid phase and gas phase for comparison. The resulting data are shown in Figure 3.3(a) and reveal that the 0.1 and 0.2 wt% Pt/TiO_2 catalysts have the best activity and the 5 wt% Pt/TiO_2 catalyst have near zero activity, in the liquid phase. Hydrogen production values for both the liquid and gas phase arrangements have not been photon-normalised.

Figure 3.3: (a) Liquid phase hydrogen production from various Pt loadings (b) Gas phase hydrogen production from various Pt loadings.

In the gas phase experiments however, Figure 3.3 (b) reveals the 0.1 and 0.5 wt% Pt/TiO_2 catalysts to have the best activity and the 5 wt% Pt/TiO_2 catalyst to have near zero activity, which is similar to the reactivity demonstrated by the same catalysts in the liquid phase, with the exception that twice as much H_2 is evolved in the same time period.

3.2.2.2   Pd Loading Dependence: Variation between Gas and Liquid Phase

The metal loading dependence for several different palladium catalysts prepared via the incipient wetness precipitation technique were tested for their photocatalytic activity in the liquid phase. The resulting data are shown in Figure 3.4 (a) and reveal the 0.1 and 0.3 wt% Pd/TiO$_2$ catalysts to have the best activity and the 5 wt% Pd/TiO$_2$ catalyst to have near zero activity in the liquid phase. From these data it is clear that the optimal weight loading for palladium shows a similar peak as the platinum catalysts already tested in the liquid phase, however the palladium catalysts do not exhibit the same reactivity, producing half as much hydrogen in the same reaction period, 6 ml in comparison to 12 ml by the 0.1 wt % Pd and Pt catalysts respectively. Hydrogen production values for both the liquid and gas phase arrangements have not been photon-normalised.
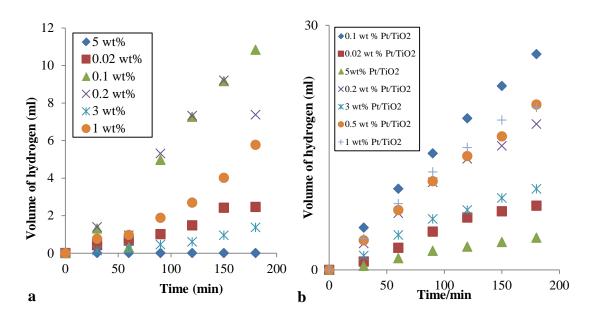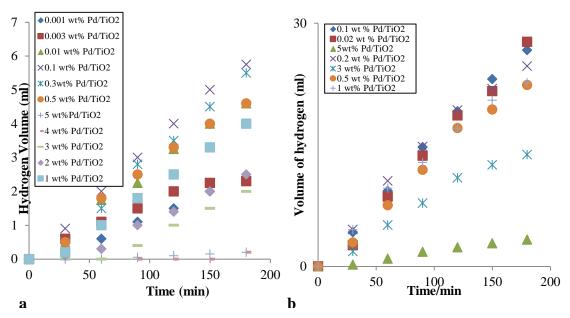

Figure 3.4: **(a) Liquid phase hydrogen production from various Pd loadings (b) Gas phase hydrogen production from various Pd loadings**

Figure 3.4 (b) reveals that there are several Pd/TiO$_2$ catalysts with similar high activities and the 5 wt% Pd/TiO$_2$ catalyst to have near zero activity again, in the gas phase, which is similar to the reactivity demonstrated by the same catalysts in the liquid phase, with the exception that almost four times as much H$_2$ is evolved in the same time period, for the palladium catalysts in the gas phase.
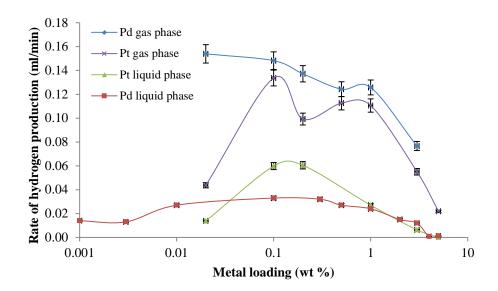

Figure 3.5: Rate of hydrogen production (ml/min) against metal weight loading for Pd/Pt catalysts in gas/liquid phase (nb: metal loading scale shown as logarithmic).

Figure 3.5 summaries the difference in reaction rate for the different weight loading of Pd/Pt catalysts in the two photocatalytic reaction phase conditions under investigation. A logarithmic scale for the metal weight loading has been utilised here to emphasis the maximum/optimal weight loading for each catalyst combination. These data clearly demonstrate that the gas phase reaction is a more effective environment for hydrogen production in comparison to the liquid phase and that the palladium catalyst is the optimal catalyst in the gas medium. Conversely, the platinum catalyst shows higher hydrogen evolution in the liquid phase.

The differing catalytic activity in the liquid phase could be due to a reduced amount of UV light reaching the catalyst in the reaction emulsion at any one time due to the catalyst suspension inducing a "shadow" effect upon itself, hence reducing the rate at which CO is

removed from the active site[2b,7]. Boudart[23] discovered a similar observation when investigating the differing activity of the catalytic hydrogenation of cyclohexene in the gas and liquid phase proposing that the additional barriers present in the liquid phase reaction, namely, mass transfer limitations, ie the resistance of H_2 movement from the gas phase, to the bulk then to the catalyst surface, could result in the lower reaction rate.

The maximum peak shown in Figure 3.5 is common to all the reaction types and is independent of the reaction phase, for both Pt and Pd the optimal weight loading of metal on titania is observed at between 0.1 - 0.2 wt% metal/titania.

Interestingly these data also suggests that there may be a double maximum, for the optimal weight loading in the gas phase, with a second peak being observed for both Pd and Pt at around 1 wt% metal loading, however further investigation would be required around this anomaly to confirm this observation to be true.

If this phenomenon was proven, this would lead one to conclude that there are two active sites present in the gas phase reaction, additionally a differing reaction mechanism between the two phases could explain the change of palladium from the lower reaction rate to the higher reaction rate on movement from the liquid to the gas phase.

The liquid phase reaction shows the expected trend, palladium behaving as a less efficient catalyst, as observed by Sachtler et al[24] for the decomposition of formic acid. Schwartz et al[25] also published results showing differing reactivity for palladium and platinum when investigating their catalytic activity for oxidation of simple organic compounds, concluding that palladium was a less efficient catalysis due to the presence of the stable oxide, PdO. Building on this, it could be possible for one to hypothesis that the gas phase mechanism may benefit from the presence of PdO but the liquid phase may be hindered by the presence of this stable oxide; however this eventuality does not prove very likely due to the reductive environment in which this reaction occurs.

3.2.2.3   High Metal Loading

A 5 wt% palladium catalyst was made and tested to clearly compare with the high metal loading platinum catalyst. These data are shown in Figure 3.6, which clearly illustrates that titania with a high palladium loading experiences an induction period and has a much higher

rate of hydrogen evolution in comparison to the equivalent weight loaded platinum catalyst, however this rate is still lower than the 0.5 wt% Pd/TiO_2 reported in Figure 3.2. Hydrogen production values for the liquid phase arrangement have not been photon-normalised.
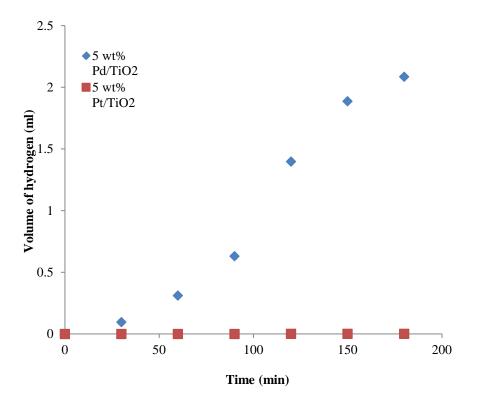

Figure 3.6: Hydrogen Production for 5 wt% Pd/TiO2 and 5 wt% Pt/TiO2 catalysts in liquid phase water/methanol system.

The induction period observed for the 5 wt% palladium catalyst is consistent with the particle growth model suggested by the Bowker group[26], for instance the slow rate at the beginning could be due to the small perimeter of the support and metal boundary available as the active site due to the high metal loading, however as the reaction progresses the aqueous catalyst dispersion could allow various Pd particles from different parts of the catalyst to touch on the support, hence increasing the vital perimeter required for the proposed mechanism resulting in an increase in the rate of reaction. As the reaction continues there is a decrease in the rate of hydrogen production, possibly due to a reduction in the number of palladium particles exposed to the $MeOH/H_2O$ system as a result of the supporting TiO_2 particles agglomerating, as seen in Figure 3.7.

The slow rate at the beginning could be due to the small perimeter of the support and metal boundary available to act as the active site described in the proposed mechanism in Figure 3.1. As the reaction continues there is a increase in the rate of hydrogen production, possibly due to smaller surface Pd particles agglomerating, increasing the number of titania/palladium active sites exposed to the MeOH/H_2O. The more even distribution of these optimised active sites in lower loading palladium supported catalysts may mask the slower hydrogen production rates displayed by the small perimeter active sites seen in higher loading giving the rates seen in Figure 3.2.
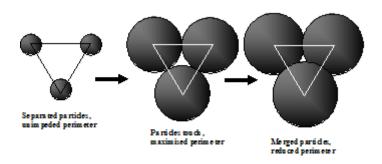

Separated particles, unimpeded perimeter

Particles touch, maximised perimeter

Merged particles, reduced perimeter

Figure 3.7: Schematic diagram from Bowker et al paper[21], showing particle growth on the titania surface, with increasing metal weight loading.

Another proposal for the reduced photoreactivity of high weight loaded titania catalysts for UV irradiated reactions has been attributed to the reduction in the amount of light irradiation being experienced and hence absorbed by the semiconductor support, due to the increased number of metal nano-particles present at the surface introducing a physical "umbrella" effect on the titania support below[27].

3.2.3   Other TiO_2 Supports

The work surrounding other phases of titania; similar to the P25 support used in the discussed weight loading studies, is widely studied and well documented in the literature[28]. The following section of experiments documents the investigation of the photocatalytic activity of the component phases present in P25 titania, namely rutile and anatase TiO_2.

3.2.3.1   Rutile Titania

Despite being the more common natural phase of titania, research of rutile's catalytic activity is less widely published than that of P25 and other mixed phase supports. One might be led to believe that this is no coincidence believing that any dip in volume of publications is due to its lack of catalytic ability but Li et al have reported the importance of the surface interaction of the rutile and anatase phases of titania in their studies of photocatalytic methanol reforming[29]. The significance of TiO_2 in the rutile phase have been further reported by Fujihara et al for its ability to split water by an electrochemical combination of two photocatalytic reactions[30, 31] and by Keller et al[32] in the catalytic oxidation of CO by visible light. These studies indicate that rutile can exhibit catalytic activity, making it an ideal support to investigate here for its photocatalytic activity in the methanol photoreforming reaction.

The first rutile catalyst to be investigated was an as received low surface area (3 m^2g^{-1}) rutile phase titania, which was dosed with 0.5 wt% Pd via the incipient wetness technique described previously. The results from this reaction are shown in Figure 3.8 and reveal that the 0.5 wt% Pd/Aldrich catalyst does not produce a measurable quantity of hydrogen in the methanol/water system. It was suggested that the Pd:TiO_2 ratio at the surface of the catalyst might have been too high resulting in the active centre, discussed earlier[26], having a low perimeter due to the low surface area of the sample. A lower percentage weight catalyst was therefore made (0.05 wt% Pd/TiO_2) and tested in the methanol reforming reaction, but this too gave no hydrogen production.

To address the problem of the low surface area of the as received rutile titania in comparison to that of the standard P25 titania supported catalyst used within the group (59 m^2g^{-1} for 0.5 wt% Pd/TiO_2) a relatively high surface area rutile titania support was synthesised following the method employed by Keller et al[32], see chapter two.
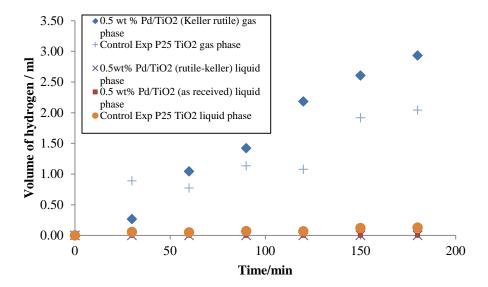
Figure 3.8: Hydrogen production by rutile supported palladium catalysts with various reaction environments.

The resulting TiO_2 was found to have a surface area of 50 m^{2}g^{-1} and when a 0.5 wt% Pd catalyst was made with this support (0.5 wt% Pd/Keller) and tested for its photocatalytic activity, the increase in surface area was found to have no effect towards its ability to produce hydrogen, see Figure 3.8.

The gas phase reaction was investigated for the as received Aldrich and synthesised Keller rutile titania and found to have no effect on the methanol reforming ability under scrutiny.

It can therefore be concluded that the rutile phase of titania when tested alone, shows similar activity to non-transition metal loaded P25 titania and by this measure is not active for the photocatalytic reaction under investigation here.

3.2.3.2 Effect of Mechanical Treatment on Rutile TiO_2

Following this ball milling was attempted to try and increase the surface area of the rutile support used. There have been several studies into the effect of ball milling and its ability to increase the surface area of catalytic oxides supports[33-35]. Further to these observations, high energy ball milling has been attributed to inducing phase transformation of anatase titania by Girot et al[36]. However, similar degradation of phase boundaries have been disproven when the initial product to undergo ball milling was 100 % rutile titania[37].

The titania compound used in the ball milling process was the as received rutile phase TiO_2 from Aldrich, samples of the titania support were periodically removed from the ball mill and tested by BET analysis to examine whether the technique had increased their surface area over 6 hours. However the support's surface area showed no movement from BET analysis of the six different samples. The samples were impregnated with Pd and the resulting catalysts tested for their catalytic activity in the methanol reforming system, confirming the non-result from the ball milling experiment.

The result is not surprising when comparing the energy of the 50 rpm ball mill used directly to the 1422 rpm equipment used in the literature[36]. It is apparent that the slow speed used in this test does not provide sufficient energy to break up the TiO_2 particles.

The lack of reactivity displayed by the rutile supported catalysts tested reflects the reduced band gap shown to be present for this phase of titania[38, 39]; these effects change the semiconductor behaviour of the catalyst, allowing direct electron transitions, which in turn accommodates rapid electron/hole recombination in comparison to the anatase phase. Rapid electron/hole recombination hinders the rate of photocatalytic reaction because the charge separation required for steady state methanol reforming cannot be maintained for long enough for the holes and electrons to intercept the reaction precursor species. Rutile phase titania has however been proven to successfully produce lots of charge carriers under UV irradiation as a result of having a lower band gap[40, 41], however without increasing the lifetime of photo-excited electron produced, the metal supported rutile titania studied here for its use in the photocatalytic methanol reforming reaction struggle to act as a reliable photocatalyst.

3.2.3.3 Anatase

Titania has been reported as an active photocatalyst in its anatase phase for many reactions including the degradation of dyes[42] and ethanol reforming[43]. It was therefore of interest to investigate the phototcatlytic ability of anatase phase TiO_2 for the methanol reforming reaction. Figure 3.9 shows the hydrogen production from 0.5 wt % platinum loaded anatase support, made from as received titania from Aldrich supplier. These data show that anatase titania alone shows promise as a catalytic support for the methanol reforming reaction.

3.2.3.4   Supercritical Anatase Titania

Following on from the rutile and anatase titania work, some anatase phase TiO_2 formed by the supercritical antisolvent process[44, 45] was provided by Raimon Perea Marín and tested for its photocatalytic ability. The two samples provided were made from different Ti precursors and both had very different surface areas, see Table 3.1.

Ti Precursor	Surface Area (m^2g^{-1})
$TiO(acac)_2$	11
Ti-isopropoxide	92
Ti-commercial	40

Table 3.1: Surface area of anatase TiO_2 prepared by the supercritical antisolvent process.

Figure 3.9 shows the differing results obtained from the photoreaction of supercritically prepared TiO_2 dosed with Pt. These data reveal that the higher surface area anatase catalyst prepared from titanium isopropoxide produced more than ten times as much hydrogen as the lower surface area anatase catalyst prepared from a $TiO(acac)_2$ precursor, an explanation for the difference in rate could be attributed to the surface area of the Ti-isopropoxide sample being almost ten times greater than that of the $TiO(acac)_2$ sample. This argument supports the observation of the Pt impregnated TiO_2 catalyst made from the Aldrich anatase precursor producing 0.35 ml of hydrogen in comparison to 0.08 ml over the reaction period from the same weight loaded $TiO(acac)_2$ precursor catalyst (Figure 3.9), a difference in hydrogen evolution, which is equivalent to the difference in surface area of the two catalysts. Vinu et al also apply this rational to explain the increase in photocatalytic degradation rate of dyes with increasing catalyst surface area of their anatase supported palladium catalysts [42].
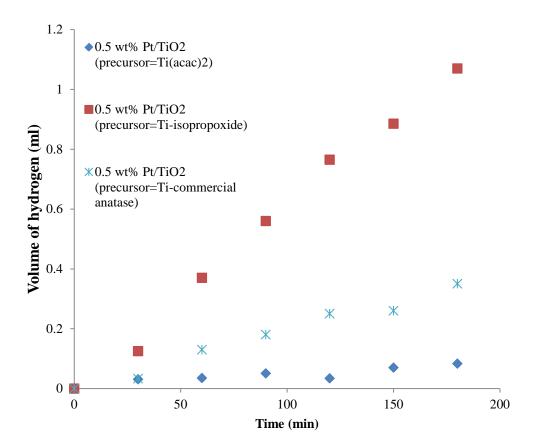
Figure 3.9: Results from the photoreaction of supercritically prepared TiO₂ dosed with Pt.

3.2.3.5   *Mixture of Supports*

The small amount of hydrogen obtained from the anatase supported catalysts, cannot make up for the activity observed from the Bowker group's standard 0.5 wt% Pd/P25 TiO$_2$, which is made up of a mixture of anatase and rutile titania (4:1). The difference in activity must therefore be attributed to the presence of the rutile phase in P25 titania used. To investigate this further physical mixtures of the rutile catalyst impregnated with 0.5 wt % Pd (rutile precursor synthesised using the Keller method[32]) and anatase or P25 TiO$_2$ were tested for their photocatalytic ability.

Figure 3.10 shows that when the Pd supported rutile titania catalyst was retested for its photo reforming ability in the presence of anatase TiO$_2$ in the liquid phase there was no improvement in hydrogen production.

However, when the Pd supported rutile catalyst was tested in the presence of P25 TiO$_2$ there was a notable improvement in hydrogen evolution both in the liquid and gas phase. For both the gas and the liquid phase reactions where a 1:1 mixture of catalyst and P25 were present the reaction yielded up to twice as much hydrogen from the same overall weight of catalyst mixture.

These data confirm the importance of the phase junction formed at the surface of TiO$_2$ between the anatase and rutile phases in P25, which has been previously reported to be a required interface for the photocatalytic reforming of methanol[29]. Jovic et al have similarly reported reduced reaction rates for the separate titania phases in comparison to P25 supported catalysts where the two phases are present[43]. In their paper they detail how the three way interface, where Au is deposited on rutile and anatase, is the optimised location for the production of hydrogen from an ethanol water reaction under UV light excitation.

These results not only suggest that such a phase boundary is necessary in the photocatalytic methanol reforming reaction being investigated here., but that a physical mixture of the anatase and rutile phases of titania is enough for a physical phase junction to occur.
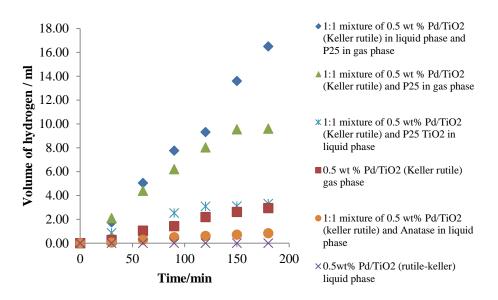

Figure 3.10: Hydrogen production by rutile supported palladium catalysts with various reaction environments.

 Perhaps most the most notable observation from these mixed support reactions, is the evolution of hydrogen where no physical junction between the P25 titania and Pd loaded rutile catalyst is present, as seen for the most productive mixture shown in Figure 3.10. For

this experiment the Pd loaded catalyst was in the liquid phase and the P25 titanium oxide was packed onto a gas phase slide, and the reaction undertaken as usual with the MeOH also in the liquid phase. An explanation for this anomaly, may simply be that a small amount of P25 titania became unstuck from its glass support in the gas phase and fell into the reaction mixture containing the Pd loaded rutile phase catalyst and the reduced ratio of P25 titania present might have increased the reaction rate.

Only 1:1 physical mixtures of the rutile catalyst and P25 titania have been investigated here, altering the ratio of the support mixtures could affect the rate of reaction observed and help confirm the above anomaly where no physical mixture was intended.

Building on these results, for the differing reactivity of palladium/platinum loaded photocatalysts prepared using rutile or anatase crystalline phase titania in comparison to one another and when used in combination in the methanol reforming reaction under investigation here, one can begin to piece together a proposal to enhance the understanding of the reaction mechanism[21, 26].

The lack of reactivity displayed by the rutile catalysts may reflect a reduced lifetime of the photo-excited electron crucial for methanol reforming, as a result of the lower band gap of the titania semiconductor support[38, 39] despite the rutile crystalline phase being a better source of photo-excited electrons than anatase under UV irradiation[40, 41]. The metal catalysts prepared using anatase precursor titania also showed reduced photoactivity in comparison to P25 supported palladium/platinum catalysts, suggesting that the presence of all three crystalline phases were necessary for hydrogen production to occur, furthermore the findings that only a physical mixture of these interfaces may be suffice to support methanol reforming and achieve high yields from the photocatalysis system. These observations along with previous results and publications from the Bowker group[3, 10, 21, 26] can be combined to propose the mechanism shown in Figure 3.11.
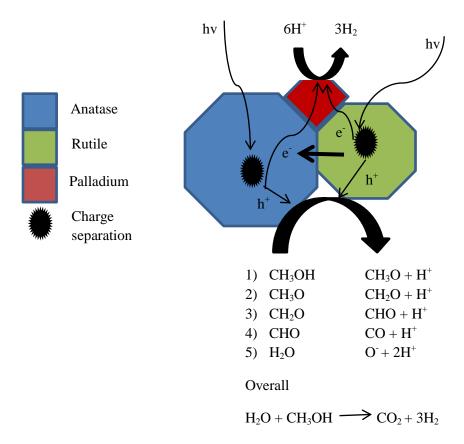
Figure 3.11: Schematic diagram showing the proposed mechanism for hydrogen evolution from photocatalytic methanol reforming upon UV irradiation.

Figure 3.11 shows the importance of the physical interface between the anatase and rutile crystalline phases of titania and palladium nanoparticles in the UV irradiated methanol reforming reaction, and has been adapted from Jovic et al proposed mechanism for UV light activated hydrogen production from an ethanol/water system in the presence of a Au loaded titania support[43].

The mechanism proposed here demonstrates the prolonged period between electron/hole recombination due to charge transfer between the rutile and anatase phases, with the advantage of these sustained charge carriers allowing the steady state oxidation of water and methanol via the holes and reduction of adsorbed H^+ ions at the cathodic palladium site to occur at the physical boundary of these interfaces.

This mechanism supports the theory proposed by the Bowker group[3, 10, 21, 26] that both surface palladium and surface titania are required, refining the model described in Figure 3.1 to include the importance of the two crystalline phases of titania must also be present at the surface to accommodate hydrogen production. Furthermore, the mechanism fits the observations of the effect of metal weight loading on the reaction rate, where increasing the

palladium/platinum weight loading on the catalyst support reduces the perimeter of the active site between the two crystalline phases and Pd/Pt, as shown by the particle growth model in Figure 3.7. Jovic et al however propose that this decrease in photocatalyst activity on increasing weight loading is due to an increase in the number of Au/rutile sites relative to the three phase 'hotspots' described in the mechanism in Figure 3.11, which causes an increase in electron/hole recombination with increasing rutile sites[43].

3.2.4   Other Sacrificial Agents

3.2.4.1   Crotonaldehyde

So far only methanol has been investigated here for its hydrogen production by reforming; in this section crotonaldehyde has been studied for its ability as a sacrificial agent in the photocatalytic reforming reaction under investigation. Crotonaldehyde is of particular interest due to the presence of two organic functional groups, a double bond and an aldehyde group, as seen in Figure 3.12, which have been studied in unpublished work within the Bowker group. Interestingly, ethene did not demonstrate any hydrogen production, whereas molecules which contained an aldehyde group did.
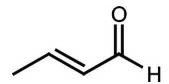

Figure 3.12: Schematic diagram of the aldehyde and double bond present in crotonaldehyde

Figure 3.13 shows hydrogen production by reforming of methanol and crotonaldehyde under UV conditions using the same 0.5 wt % Pd impregnated P25 support. These results show that for the reaction conditions under investigation here, crotonaldehyde is an unsuccessful sacrificial agent for the production of hydrogen and demonstrates the same reactivity as the control experiment where no organic agent is present in the reaction mixture. Similarly, when ethene did not evolve any hydrogen when it was substituted for methanol in the photocatalytic reforming system, it has been hypothesised that the lack of activity demonstrated by ethene and crotonaldehyde may be due to the double bond poisoning the

Pd/TiO$_2$ catalytic surface, since ethene has been shown to have a strong affinity to the Pd (110) surface at ambient temperatures[46], as per the mechanism in Figure 3.1 the sticking probability exerted by the double bond in crotonaldehyde may be too strong to be desorbed upon UV light irradiation, hence poisoning the catalyst surface and preventing hydrogen evolution to occur.
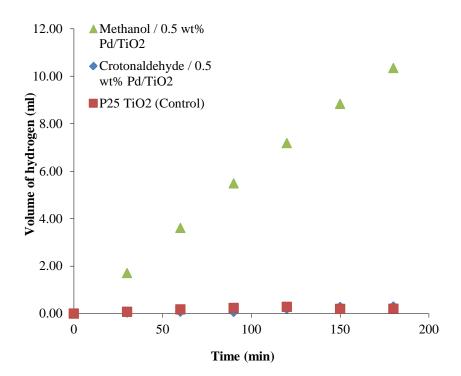

Figure 3.13: Hydrogen production from the photocatalytic reforming of crotonaldehyde using a 0.5 wt % Pd/TiO$_2$ catalyst in the liquid phase.

3.3   Conclusion

Several topics have been investigated here towards hydrogen production by photocatalysed reforming of methanol, mainly the effect of metal weight loading on the titania support and the dependence of the crystallite phase of the titania pre-cursor.

The palladium/platinum weight loading dependence in the gas and liquid phase showed that independent of the phase of reaction, the amount of hydrogen produced from methanol reforming irradiated by UV light decreased for increasing metal weight loading. Additionally

the gas phase reaction was found to be a more efficient environment to facilitate the methanol reforming reaction than the liquid phase, where platinum demonstrated higher hydrogen evolution in the liquid phase compared to palladium in the liquid phase but the reverse observation was seen in the gas phase reactions.

Following this the reactivity of rutile and anatase phase titania supported palladium/platinum catalysts were tested for their ability to produce hydrogen in the methanol reforming reaction, both phases were found to be poor photocatalysts alone but upon combination both chemically in the P25 based catalysts and in physical mixtures, where Pd was present on only the rutile phase, the amount of hydrogen produced was improved. This observation along with previous findings in the group was used to propose a refined mechanism for the methanol reforming reaction occurring at the surface of the Pd/Pt TiO$_2$ catalyst. Highlighting the importance of both rutile and anatase phases being present at the actives sites, where hydrogen evolution occurs at the surface of the catalyst surface.

Finally, the photocatalytic system was tested for its ability to produce hydrogen using a different sacrificial organic agent, crotonaldehyde, and these results showed no activity, which could be a result of the double bond present in crotonaldehyde poisoning the catalyst surface, preventing hydrogen evolution from occuring.

3.4 References

1.   A. Fujishima and K. Honda, *Nature*, 1972, **238**, 37-+.

2.   I. Rossetti, *ISRN Chemical Engineering*, 2012, **2012**, 21.

3.   M. Bowker, P. R. Davies and L. S. Al-Mazroai, *Catalysis Letters*, 2009, **128**, 253-255.

4.   N. Luo, Z. Jiang, H. Shi, F. Cao, T. Xiao and P. P. Edwards, *international journal of hydrogen energy*, 2009, **34**, 125-129.

5.   V. M. Daskalaki and D. I. Kondarides, *Catalysis Today*, 2009, **144**, 75-80.

6.   T. Kawai and T. Sakata, 1980.

7.   T. Kida, G. Guan, N. Yamada, T. Ma, K. Kimura and A. Yoshida, *International journal of hydrogen energy*, 2004, **29**, 269-274.

8.   A. Dickinson, University of Reading, 1997.

9.   M. Bowker, D. James, P. Stone, R. Bennett, N. Perkins, L. Millard, J. Greaves and A. Dickenson, *Journal of Catalysis*, 2003, **217**, 427-433.

10.   M. Bowker, L. Millard, J. Greaves, D. James and J. Soares, *Gold Bulletin*, 2004, **37**, 170-173.

11.   A. L. Linsebigler, G. Q. Lu and J. T. Yates, *Chemical Reviews*, 1995, **95**, 735-758.

12.   M. Ni, M. K. H. Leung, D. Y. C. Leung and K. Sumathy, *Renewable & Sustainable Energy Reviews*, 2007, **11**, 401-425.

13.   D. James, University of Reading, 1999.

14.   L. Millard, University of Reading, 2003.

15.   J. Greaves, University of Reading, 2005.

16.   L. S. Almazroai, University of Cardiff, 2009.

17.   T. Chen, Z. Feng, G. Wu, J. Shi, G. Ma, P. Ying and C. Li, *Journal of Physical Chemistry*, 2007, **111**, 8005-8014.

18.   B.-S. Huang, F.-Y. Chang and M.-Y. Wey, *International journal of hydrogen energy*, 2010, **35**, 7699-7705.

19.   V. Balzani, L. Moggi, M. F. Manfrin, F. Bolletta and M. Gleria, *Science*, 1975, **189**, 852-856.

20.   H. B. Gray and A. W. Maverick, *Science*, 1981, **214**, 1201-1205.

21.   A. Dickinson, D. James, N. Perkins, T. Cassidy and M. Bowker, *Journal of Molecular Catalysis A: Chemical* 1999, **146**, 211-221.

22.   D. W. James, University of Reading, 1998.

23.   E. E. Gonzo and M. Boudart, *Journal of Catalysis*, 1978, **52**, 462-471.

24.   W. M. Sachtler, G. J. H. Dorgelo, Fahrenfo.J and Voorhoev.Rj, *Recueil Des Travaux Chimiques Des Pays-Bas*, 1970, **89**, 460-&.

25.   A. Schwartz, L. L. Holbrook and H. Wise, *Journal of Catalysis*, 1971, **21**, 199-207.

26.   M. Bowker, D. James, P. Stone, R. Bennett, N. Perkins, L. Millard, J. Greaves and A. Dickinson, *Journal of Catalysis*, 2003, **217**, 427-433.

27.   X. Zhang, Y. L. Chen, R. S. Liu and D. P. Tsai, *Reports on progress in physics. Physical Society (Great Britain)*, 2013, **76**, 046401.

28.   M. Bowker, *Green Chemistry*, 2011, **13**, 2235-2246.

29.   J. Zhang, Q. Xu, Z. Feng, M. Li and C. Li, *Angewandte Chemie-International Edition*, 2008, **47**, 1766-1769.

30.   K. Fujihara, T. Ohno and M. Matsumura, *Journal of the Chemical Society, Faraday Transactions*, 1998, **94**, 3705-3709.

31.   T. Ohno, D. Haga, K. Fujihara, K. Kaizaki and M. Matsumura, *The Journal of Physical Chemistry B*, 1997, **101**, 10605-10605.

32.   F. Bosc, A. Ayral, N. Keller and V. Keller, *Applied Catalysis B-Environmental*, 2007, **69**, 133-137.

33.   D. Bork and P. Heitjans, *Journal of Physical Chemistry B*, 1998, **102**, 7303-7306.

34.   S. Indris and P. Heitjans, in *Metastable, Mechanically Alloyed and Nanocrystalline Materials, Pts 1 and 2*, eds. J. Eckert, H. Schlorb and L. Schultz, Trans Tech Publications Ltd, Zurich-Uetikon, 2000, vol. 343-3, pp. 417-422.

35.   S. Indris, D. Bork and P. Heitjans, *Journal of Materials Synthesis and Processing*, 2000, **8**, 245-250.

36. T. Girot, S. Begin-Colin, X. Devaux, G. Le Caer and A. Mocellin, *Journal of Materials Synthesis and Processing*, 2000, **8**, 139-144.

37. J. L. Guimaraes, M. Abbate, S. B. Betim and M. C. M. Alves, *Journal of Alloys and Compounds*, 2003, **352**, 16-20.

38. A. K. Ghosh, F. G. Wakim and R. R. Addiss, *Physical Review*, 1969, **184**, 979-&.

39. N. Serpone, D. Lawless and R. Khairutdinov, *Journal of Physical Chemistry*, 1995, **99**, 16646-16654.

40. D. C. Hurum, A. G. Agrios, S. E. Crist, K. A. Gray, T. Rajh and M. C. Thurnauer, *Journal of Electron Spectroscopy and Related Phenomena*, 2006, **150**, 155-163.

41. D. C. Hurum, A. G. Agrios, K. A. Gray, T. Rajh and M. C. Thurnauer, *Journal of Physical Chemistry B*, 2003, **107**, 4545-4549.

42. R. Vinu and G. Madras, *Journal of Molecular Catalysis a-Chemical*, 2008, **291**, 5-11.

43. V. Jovic, W. T. Chen, D. Sun-Waterhouse, M. G. Blackford, H. Idriss and G. I. N. Waterhouse, *Journal of Catalysis*, 2013, **305**, 307-317.

44. G. J. Hutchings, J. A. Lopez-Sanchez, J. K. Bartley, J. M. Webster, A. Burrows, C. J. Kiely, A. F. Carley, C. Rhodes, M. Havecker, A. Knop-Gericke, R. W. Mayer, R. Schlogl, J. C. Volta and M. Poliakoff, *Journal of Catalysis*, 2002, **208**, 197-210.

45. Z. R. Tang, J. K. Edwards, J. K. Bartley, S. H. Taylor, A. F. Carley, A. A. Herzing, C. J. Kiely and G. J. Hutchings, *Journal of Catalysis*, 2007, **249**, 208-219.

46. M. Bowker, C. Morgan, N. Perkins, R. Holroyd, E. Fourre, F. Grillo and A. MacDowall, *Journal of Physical Chemistry B*, 2005, **109**, 2377-2386.

Chapter 4 – Surface Science of Pd (110) and Pd/TiO$_2$ (110)

Contents

4   Introduction

Chapter one described the complexity and unique structure present at the surface of a 'rough' solid at an atomic level, with each individual deviation from uniformity at the surface lending different electronic properties, contributing towards an unreproducible surface composition to study. Therefore to undergo reproducible experimentation into the properties of a catalyst and how its surface behaviour influences a reaction, one must revert back to a simplified system in order to build upwards to propose the mechanism at play. By employing a well-defined surface, created by cutting through a crystal at a particular crystal plane, the complexity displayed at the surface of a 'rough' solid can be introduced by adding controlled amounts of surface defects and coverages of distinguishable adsorbates, to create a model environment.

This section of the project focuses on work conducted in a UHV system investigating the surface science behaviour of oxygen on Pd (110), in a hope to generate a more concise mechanism of oxygen's role in the photocatalysised methanol reforming system discussed in chapter three.

There is also a brief section describing molecular beam experiments of crotonaldehyde on Pd (110), which has been chosen as it is a model oxygenate molecule, whose surface interaction and reaction could give clues to methanol's behaviour on the powdered catalyst.

The concluding section of this study documents the preparation of a model Pd/TiO_2 to replicate the surface environment of the powdered catalysts used in the photocatalytic methanol reforming reaction used in chapter three.

4.1   Results and Discussion

4.1.1   Palladium (110)

To aid our understanding of the importance of palladium in the methanol reforming reaction, a palladium crystal cut to expose the (110) plane of the face centred cubic (fcc) array, and will act as the well-defined atomic surfaces onto which O_2 and acetaldehyde sticking probabilities have been studied. Pd (110) is the least closely packed of the three common fcc

planes, resulting in the surface having the highest surface energy and hence is considered the most reactive palladium crystal surface plane.

4.1.1.1 Oxygen Absorption/Adsorption

Oxygen reactivity on well-defined metal crystal surfaces is a heavily published area of surface science due to its simplicity and importance in even the most fundamental chemical reactions and has been reviewed by Lundgren et al for late transition metals such as palladium[3]. Oxygen has previously been shown to dissociatively adsorb onto Pd (110) for temperatures greater than 160 K[4, 5] and molecularly at temperatures lower than 160 K[6]. He et al have identified subsurface oxygen upon thermal desorption[7-9], building on research by Weissman-Wenocur et al who reported oxygen migration into the bulk in their surface studies on Pd(111)[10]. The structures formed on these palladium close packed surfaces are of particular interest to the Bowker group due to their relevance to heterogeneous catalysis, particularly oxygen's role in the photocatalysised methanol reforming reaction

Molecular beam experiments involving oxygen were conducted using the in house molecular beam reactor described in chapter two, for these experiments the mass spectrometer was set to record partial pressures of carbon monoxide, carbon dioxide and oxygen. Changes to the oxygen beam profile were recorded to monitor the change in the sticking probabilities associated with the opening and closing of the molecular beam flag, when the beam flag is opened, the crystal is subject to a constant exposure of O_2 molecules, whereas when the beam is closed the beam is interrupted and no longer hits the sample.

Figure 4.1 shows the molecular beam profiles from this group of experiments, a slight increase in the carbon monoxide partial pressure was observed upon opening the beam to and for experiments conducted where the Pd (110) surface was at 773 K the mass spec analysis showed continuous production of CO and CO_2, which can be attributed to the cleaning of C from the surface of the palladium. For these reasons temperatures below 773 K were employed throughout the course of this study since apart from an increase in the background pressure of CO at mass 28 there was no significant increase in CO or CO_2 partial pressure during opening and closing of the beam flag.
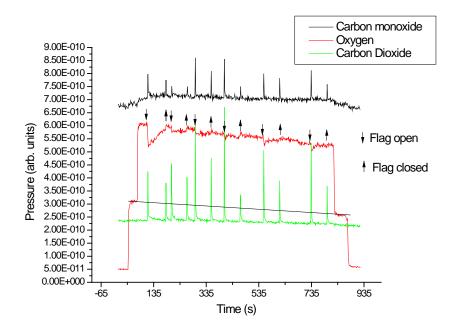
Figure 4.1: Oxygen beam profile conducted at 473 K with varying flag closure periods for Pd (110) annealed to 773 K

The molecular beam profile, detailed in Figure 4.1, shows the variation in adsorption over time for prolonged exposure of the Pd(110) surface to a beam of oxygen molecules. These profiles, were converted into sticking probabilities using the procedure described in section 2.2.4.1 in chapter two and show a high initial O_2 sticking probability (~0.3 +/- 0.02) for the first flag opening period, which eventually drops off, suggesting the palladium surface, is becoming saturated, i.e. no further O_2 sticking is occurring. Following a brief flag closure (between 175 s and 205 s on the beam profile) the surface is exposed to the O_2 beam, the beam profile observed for this second flag opening displays a significantly different pattern, whereby the O_2 sticking probability is constant (between 205 s sand 265 s on the beam profile), suggesting that a steady state of oxygen adsorption is occurring, i.e. a constant amount of oxygen is being adsorbed due to migration of the dissociated oxygen into the subsurface/bulk.

It was noted that altering the flag closure periods between direct exposure of the O_2 beam to the Pd (110) surface affected the sticking probability recorded, with the sticking recorded directly following flag opening and consequently O_2 beam exposure, increased as the flag closure period increased. These observations have been quantified and can be seen in Figure 4.2. These data show the initial sticking probability experienced by the O_2/Pd (110) system

following flag opening and its decrease over a 60 second exposure window; the sticking probability grew with increasing flag closure periods, suggesting that the longer the palladium surface was not incident to the oxygen beam, more of the already adsorbed oxygen atoms were able to undergo migration into the bulk, since there was no CO or CO_2 evolved over the period of reaction. This trend was observed for every increase in beam flag closure period until eventually the sticking probability was encroaching on the initial beam opening measurement.
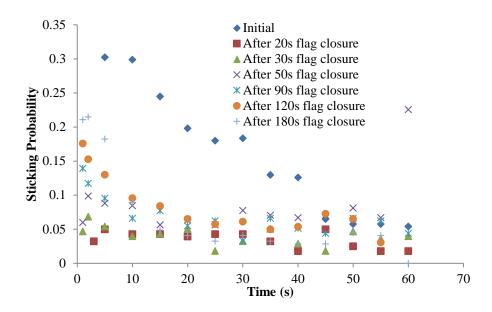

Figure 4.2: Pd (110) annealed to 300C with O2 beamed at 200C and varying flag closures

Further experiments were conducted at different anneal and experiment temperatures with a constant experiment and anneal temperature respectively, as previous research within the Bowker group has shown the effect of annealing and reaction temperature of adsorbate and surface interaction mechanisms[11]. These temperature differences didn't affect the sticking probability after short flag closures, however the main differences in O_2 sticking became more apparent as the flag closure period increased, as seen in Figure 4.3 where different gradients can be observed for charts of initial s_0 against flag closure time at different anneal and reaction temperatures.
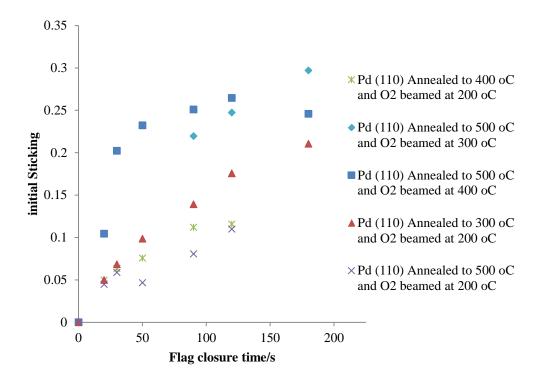
Figure 4.3: Graph to show initial sticking vs flag closure period

Figure 4.4 shows these observations as a graph of $t_{0.15}$, i.e. the length of flag closure until an s_0 of 0.15 (about midway of the slope of s_0 vs flag closure time observed in Figure 4.3) was measured upon reopening the flag. From these data it was found that for a constant experiment temperature of 473 K $t_{0.15}$ increased with increasing annealing temperature; however the opposite was found when the annealing temperature remained the same at 773 K, $t_{0.15}$ decreased with increasing experiment temperature.
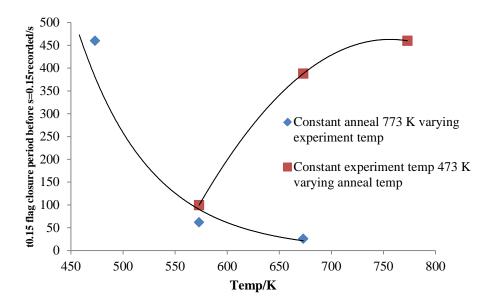
Figure 4.4: Graph to show t0.15 vs temp.

The extra uptake of oxygen is probably a result of the adsorbed O atoms migrating into the subsurface or the bulk of the crystal. If this hypothesis is true, migration might be happening more quickly at higher experiment temperatures, exposing more surface sites for adsorption to occur, hence the decrease in $t_{0.15}$. The opposite effect with $t_{0.15}$ increasing with increasing anneal temperature, which suggests that the anneal temperature may affect vacancy availability in the bulk and impede $O_{(a)}$ migration for higher anneal temperatures for the Pd (110) crystal.

Figure 4.5 shows an XP spectra of the Pd (110) in an O_2 rich environment did not detect the presence of PdO suggesting that diffuses into the bulk. He et al showed oxygen diffusion into subsurface layers[7-9], although PdO has been observed at high oxygen exposures ($p_{o2} = 4.0 \times 10^{-2}$ mbar for 20 min) by Bondzie et al[12].
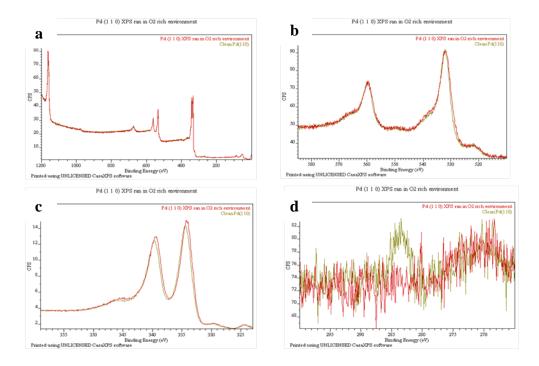
Figure 4.5: XPS of Pd (110) in an O$_2$ rich environment and clean Pd (110). Clockwise from top right (a) shows a wide scan of the Pd(110) crystal and close up spectra of (b) O 1s (c) Pd 3d and (d) C 1s.

4.1.1.2 Reactivity with Crotonaldehyde

Due to the complex nature of the photocatalytic system of interest to the Bowker group, the surface science approach of studying simple organic molecules, with low functionality has been applied here in a hope to build a fundamental understanding of the mechanisms involved. Previous studies in the Bowker group have studied how simple carbonaceous molecules adsorb onto individual components of the Pd/TiO$_2$ catalyst employed in the photocatalytic methanol reforming reaction. These studies have shown acetaldehyde to be a reactive on Pd (110)[13], around 300 K complete decarbonylation of acetaldehyde occurs to give gas phase methane and CO. For temperatures above 473 K the reaction mechanism switches to dehydrogenation whereby CO and H$_2$ are the only products evolved in the gas phase, carbon lost from the methyl group being lost by diffusion into the bulk. Similarly with other simple organic molecules, such as ethene, Pd (110) has been reported to be a "carbon sponge"[14].

With these findings in mind and the lack of reactivity reported in chapter three, crotonaldehyde was picked as simple organic molecule to probe by molecular beam sticking

experiments, to understand the effect of combining two functional groups previously studied in the Bowker group and shown to have high sticking probabilities on Pd (110), namely the double bond present in the ethene studies and the aldehyde group in the acetaldehyde body of research. Furthermore, the reaction of crotonaldehyde over a Au/Pd (111) system[15] has been reported to display similar decarbonylation and dehydrogenation properties as per those exhibited by Pd (110) in the presence of acetaldehyde[13]. Previous research also details how Pd surface displays selective hydrogenation towards the two functionalities present in crotonaldehyde[16].
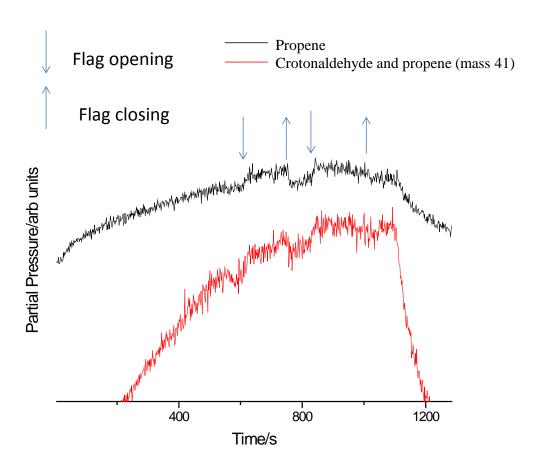

Figure 4.6: Molecular beam profile of crotonaldehyde beamed at 323 K onto clean Pd (110) annealed to 873 K. N.B. partial pressure measured at mass 41 is common to cracking mass of propene and crotonaldehyde.

For these experiments the mass spectrometer was set to record partial pressures of carbon monoxide, carbon dioxide and oxygen, hydrogen, propene-42 and propene/crotonaldehyde-41. Figure 4.6 shows the profile of crotonaldehyde beamed onto Pd (110) which had been annealed to 873 K. These profiles show the evolution of propene (mass 42 and mass 41) upon

crotonaldehyde exposure, CO and H_2 evolution were also observed but are not displayed in Figure 4.6, these observations suggest that the decarbonylation of the adsorbed aldehyde is occurring at the palladium surface.

These molecular beam studies were repeated for increased reaction temperatures to monitor the effect these changes had on the reaction mechanism and the beam profiles can be observed in Figure 4.7 for Pd (110) at 473 K. These profiles display the evolution of only H_2 and CO into the gas phase, suggesting that full dehydrogenation is occurring at reaction temperatures elevated from the ambient.
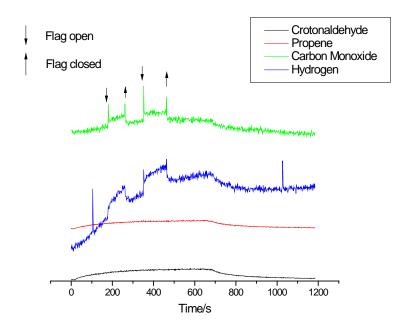

Figure 4.7: Pd (110) annealed to 873 K for 5 min and crotonaldehyde beamed at 473 K.

There were a lot of difficulties encountered trying to conduct these due to the relatively high molecular weight of crotonaldehyde and its high magnitude to stick to the stainless steel walls of the reaction chamber, which creating difficulties in beaming the molecules and reproducing these results. At a high level, these data show similar data to previous group studies into the reactivity of Pd (110) towards low functionality organic molecules, where decarbonylation of crotonaldehyde was observed for ambient reaction temperatures, Eq[n] 4.1 and dehydrogenation of crotonaldehyde at elevated temperatures, Eq[n] 4.2.

$$CH_3CHCHCHO \rightarrow CH_3CHCH_2 + CO \qquad\qquad \text{Eq}^n\ 4.1$$

$$CH_3CHCHCHO \rightarrow CO + 3H_2 + 3C \qquad\qquad \text{Eq}^n\ 4.2$$

4.1.2   Pd/TiO$_2$ - Model Catalyst Pd Growth on TiO$_2$ (110)

The surface studies in the Bowker group previously and here have focussed on the mechanism of organic reactions and surface behaviour of Pd (110) providing a foundation for understanding the mechanism of the methanol reforming reaction detailed in chapter three. To develop these theories and build direct comparisons to the mechanisms proposed in chapter three, a model catalyst surface was produced by metal vapour deposition (MVD), to recreate the surface properties present in the powdered palladium catalysts used in the photocatalysis study.

Deposition of palladium on TiO$_2$ (110) was carried out using the MVD technique and settings described in chapter two, the progress and identification of palladium growth was monitored by XP Spectra to give a detailed description of the catalyst surface produced. The amount of Pd dosed was directly regulated by the duration of deposition from the small aperture of the in house metal vapour evaporator used to deposit palladium and its close proximity to the crystal surface during dosing (~ 5 cm) and the constant flux of Pd atoms. All dosing experiments were performed at room temperature, with all results recorded using XPS.

Palladium dosing was carried out in controlled stages, with five initial dosing periods of 30 seconds, followed by two periods of 15 seconds and finally three prolonged dosing periods of 45 seconds, 70 seconds and 90 seconds, until a total dosing time of 375 seconds was clocked. XP spectra were recorded between each dosing period, to accurately monitor the growth of Pd on the titania surface, including close up spectra of the Pd 3d, Ti 2p, O 1s and C 1s regions, with particular emphasis being employed on the XPS signals for the dominant Pd and Ti regions. The C 1s and O 1s regions were recorded to ensure the surface remained clean of any background contaminants during the deposition procedures. The O 1s spectra won't be utilised for any quantitative analysis due to the fact that during the growth of the Pd overlayer, the Pd 3p$_{3/2}$ peak that emerges at a binding energy of 531 eV directly overlaps with the O 1s peak at 532 eV, making direct analysis of this particular region complicated.
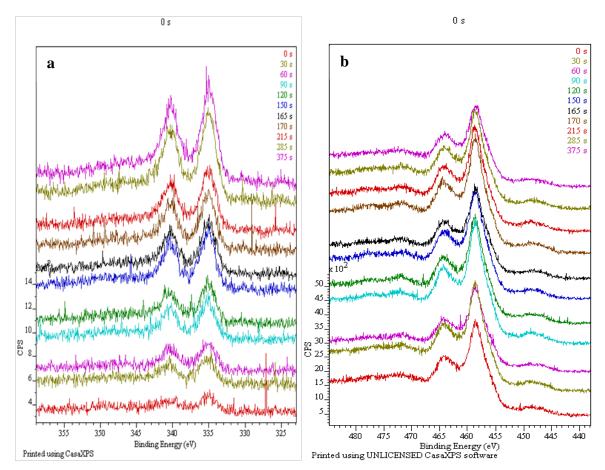
Figure 4.8: XPS spectra to illustrate the change in the Pd 3d (a) and Ti 2p (b) peaks as a function of increasing Pd dose time. The two peaks in (b) at higher binding energies (477.5 eV and 472 eV) than the main Ti 2p peaks are satellites that have arisen from charge transfer and exciton processes[1, 2]

Figure 4.8 illustrates the changes in the Pd 3d (a) and Ti 2p (b) peaks as a function of Pd deposition time; note that a small amount of residual Pd (0.6 MLs) from previous experiments is observable in the Pd 3d region. The binding energies of the palladium and titanium peaks do not shift upon increasing palladium deposition, indicating that the Pd peaks remain metallic in nature, with no reduction of TiO_2 indicating no charge transfer between the Pd adsorbate and the titania substrate[17]. Figure 4.8 also highlights the growth of the Pd 3d peaks with respect to increasing deposition time, as would be expected, but fails to demonstrate the expected reduction in Ti 2p peak intensity with prolonged deposition period, suggesting that only a small amount of surface palladium has been deposited. Through quantitative analysis of the integrals of the palladium and titanium peaks shown in Figure 4.8 one can deduce which growth mechanism is occurring during the deposition of surface palladium onto TiO_2 (110).

There are three main growth mechanisms known for metal deposition on a supporting crystal, namely, Volmer-Weber (VW), Frank-van der Merwe (FM) and Stranski-Krastanov (SK) all of which were first reviewed by Ernst Bauer in 1958[18] and have since undergone challenge and consequential expansion into the growth modes understood today.

Thin film growth from vapour deposition is governed by the strength of the interaction between the adsorbed metal atoms and the crystal surface; when the adatom/adatom interaction is stronger than the adatom/surface interaction, the surface metal forms islands this is known as VW growth and has been identified as the growth mechanism that surface palladium develops by on TiO_2[19, 20]. Conversely, FM growth occurs when the adatom/surface interaction dominates and a complete, atomically smooth layer is initially formed with further metal deposition resulting in layer by layer growth[21, 22]. The Stranski-Krastanov (SK) growth mode is a combination of the afore mentioned processes where thin film growth initially occurs in FM like 2D layers before a critical layer thickness is reached, at which point further thin film growth occurs in 3D islands upon the initial deposited 2D layers[23].
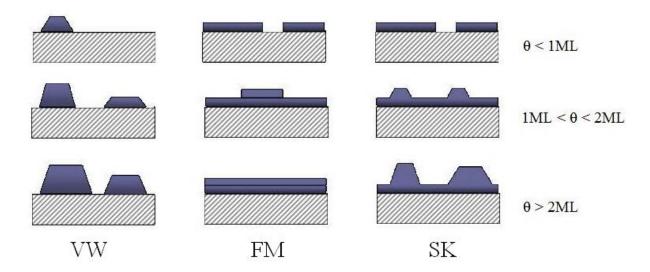

Figure 4.9: The three basic modes of thin film growth from vapour deposition. The stages of each particular growth mode are indicated by the surface coverages depicted on the right hand side of the diagram. SK growth has been simplified into 1ML of 2D layer growth

Figure 4.9 schematically details the three basic modes of metal growth, whereby VW can be simplified to 3 dimensional growth, FM 2 dimensional growth and SK a combination of 2D and 3D growth.

As mentioned, the relationship of the dominant vapour deposited metal and substrate metal XPS peaks can be utilised to identify which growth method is present by monitoring the intensity of the adsorbate/substrate XP signals against deposition time (XPS Signal-*t*), in a similar fashion to Auger signal versus deposition time (AS-*t*) plots[24]; these XPS plots can be solely used to identify the growth mechanism[25] or in conjunction with other surface sensitive techniques[26].
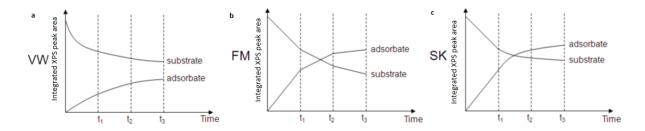

Figure 4.10: Diagram to illustrate how variations in XPS peak intensity as a function of layer thickness can be utilised to elucidate the mechanism of thin film growth. t1, t2 and t3 represent the times taken for completion of the first, second and third adsorbate

Figure 4.10 details the three differently shaped XPS Signal-*t* plots output for the three growth modes. The integrated XPS signals for the VW growth mechanism (Figure 4.10a), shows a smooth decay of the substrate XPS signal with the simultaneous smooth increase of the adsorbate XPS peak intensity at a slower rate in comparison to the FM growth mechanism. The FM growth mode is characterised by a series of linear segments of differing gradient, with the relatively sharp changes in gradient directly corresponding to the completion of a monolayer of adsorbate upon the substrate. The SK growth mechanism is a mixture of the VW and FM plots, with one or two linear segments associated with the initial layer by layer growth, before the more gradual monotonic change is observed from the subsequent bulk crystalline growth.

The qualitative integrals of the Pd and Ti peaks recorded in Figure 4.8 were used to identify the growth mechanism detailed above and are shown in Figure 4.11. The linear increase in palladium XPS signal following metal vapour deposition suggests that the Pd growth on the titania single crystal is occurring via the VW, 3D island growth model. The lack of reduction in the Ti intensity however demonstrates that although the surface Pd is increasing it is not at a high enough concentration to affect the Ti intensity. The surface Pd concentration can be

calculated using the Carley-Roberts equation to quantify the peaks recorded in the XP spectra and confirm the comparative amount of palladium present on the TiO_2 (110) surface.
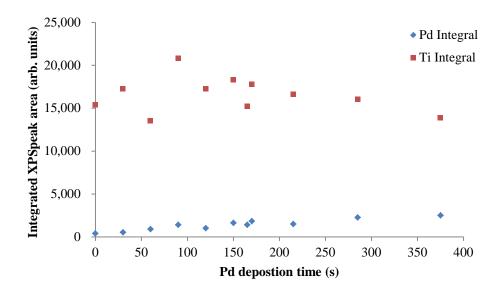

Figure 4.11: Integrated areas of the Pd 3d and Ti 2p peaks vs. Pd deposition time.

Equation 4.3 details the Carley-Roberts[27] adaptation of the equation postulated by Madley et al[28] in 1973 and can be used to calculate the surface concentration of adsorbates on a surface.

$$\square = \frac{I_A KE_A \square_s \square_s N_A \square_s \cos\square}{I_S KE_S \square_A M_S}$$

Eq^n 4.3

∇ = surface concentration, I = integrate peak intensity, KE = kinetic energy, $\searrow$ = modified photoionisation cross-section, $\leftarrow$ = photoelectron take-off angle, N = Avogadro's number, $\swarrow_s$ = escape depth of the photoelectrons through substrate, M_s = molar mass of substrate, $\triangle_s$ = substrate density, A = adsorbate and S = substrate.

Since many of the terms are constants for particular adsorbate-substrate systems; the modified photoionisation cross-section, μ, have been calculated and derived by J. H. Scofield from x-ray mass absorption coefficients[29] and the calculated values for the escape death of electrons of different energies can be obtained from data tables created by D. R. Penn[30]. Equation 4.3 can be simplified to give equation 4.4.

$$\square_A = (I_A/I_S)\, \acute{}\, A \qquad\qquad \mathbf{Eq^n\ 4.4}$$

where A= is the simplified constant for a particular adsorbate-substrate sample and has been calculated to be 2.623×10^{15} for the Pd on titania system.

Thus, by manipulating the integrated peak intensities for the Pd 3d and Ti 2p peaks respectively and employing Chang and Thornton's definition of 1ML coverage of deposited palladium[31], as one Pd atom for every exposed titanium and oxygen atom on the $TiO_2(110)$ surface ($\sim 1.516 \times 10^{15}$ atoms cm^{-2}) one can accurately calculate the surface coverage of palladium as a function of metal vapour deposition time.
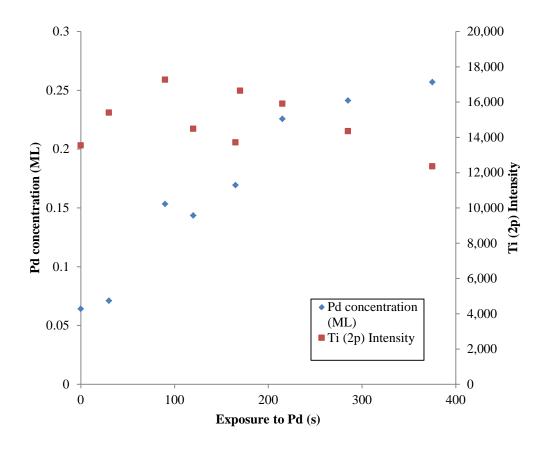

Figure 4.12: Surface Pd concentration in ML and change in Ti (2p) intensity after metal vapour deposition.

Figure 4.12 shows the increase in surface Pd with respect to increasing exposure to metal vapour deposition and the relative stability of the Ti 2p peak intensity, confirming the earlier

observation of their only being a minimal amount of surface palladium deposited on the oxide surface following deposition, only 0.26 ML after 375 s exposure to vaporised palladium.

Molecular beam experiments on the model Pd/TiO$_2$ catalyst were attempted, to probe the proposed mechanism described in Chapter three, after several low temperature annealing experiments (no higher than 473 K) showed the surface palladium to be stable enough to not undergo sintering. However molecular beam measurements on the model catalysts of Pd particles on TiO$_2$ (110) showed no sticking for several molecules, including acetaldehyde, O$_2$, ethene and CO. This was attributed to there being insufficient coverage of palladium present at the surface of the catalyst to enable good measurements to be made.

4.2 Conclusions

The surface reactivity of Pd (110) has been reported here, in particular that of oxygen adsorption and its behaviour once adsorbed on the well-defined surface. Oxygen was found to dissociatively adsorbed onto the surface of the Pd (110) crystal An initially high sticking probability was recorded on the Pd surface following the initial exposure to an incident beam of O$_2$ which dropped dramatically following a brief interruption in the incident beam. As the interruption between beam exposure points was increased the initial sticking probability increased, encroaching upon the initial sticking probability observed at the beginning of the experiment. These measurements were repeated for different reaction temperatures and different Pd anneal temperatures. It was proposed that migration of adsorbed oxygen atoms into the bulk of the crystal was happening more quickly at higher experiment temperatures, exposing more surface sites for adsorption to occur.

Next the reactivity of crotonaldehyde on the Pd (110) was studied, being of importance due to the presence of a double bond and aldehyde group in this simple organic molecule. Despite encountering difficulty reproducing the reaction, the observations recorded where in line with previous studies expectations, where decarbonylation was observed for ambient reaction temperatures and dehydrogenation at elevated temperatures.

Finally production of a model Pd/TiO$_2$ (110) catalyst was attempted and molecular beam studies carried out on the resulting surface created. Successful palladium growth by the

Volmer-Weber island growth mode were reported, however the surface palladium concentration was too low for molecular sticking reactions to be carried out on the surface.

4.3   References

1.   M. Oku, *Japanese Journal of Applied Physics Part 1-Regular Papers Short Notes & Review Papers*, 1993, **32**, 4377-4379.

2.   M. Oku, K. Wagatsuma and S. Kohiki, *Physical Chemistry Chemical Physics*, 1999, **1**, 5327-5331.

3.   E. Lundgren, A. Mikkelsen, J. N. Andersen, G. Kresse, M. Schmid and P. Varga, *Journal of Physics-Condensed Matter*, 2006, **18**, R481-R499.

4.   J. Goschnick, M. Wolf, M. Grunze, W. N. Unertl, J. H. Block and J. Loboda-Cackovic, *Surface Science*, 1986, **178**, 831-841.

5.   T. Matsushima, *Surface Science*, 1985, **157**, 297-318.

6.   L. Hanley, X. Guo and J. T. Yates Jr, *The Journal of Chemical Physics*, 1989, **91**, 7220.

7.   J. W. He and P. R. Norton, *Surface Science*, 1988, **204**, 26-34.

8.   J. W. He, U. Memmert and P. R. Norton, *Journal of Chemical Physics*, 1989, **90**, 5088-5093.

9.   J. W. He, U. Memmert, K. Griffiths and P. R. Norton, *Journal of Chemical Physics*, 1989, **90**, 5082-5087.

10.   D. Weissman-Wenocur, M. Shek, P. Stefan, I. Lindau and W. Spicer, *Surface Science*, 1983, **127**, 513-525.

11.   I. Z. Jones, R. A. Bennett and M. Bowker, *Surface science*, 1999, **439**, 235-248.

12.   V. A. Bondzie, P. Kleban and D. J. Dwyer, *Surface Science*, 1996, **347**, 319-328.

13.   M. Bowker, R. Holroyd, N. Perkins, J. Bhantoo, J. Counsell, A. Carley and C. Morgan, *Surface Science*, 2007, **601**, 3651-3660.

14.   M. Bowker, C. Morgan, N. Perkins, R. Holroyd, E. Fourre, F. Grillo and A. MacDowall, *The Journal of Physical Chemistry B*, 2005, **109**, 2377-2386.

15.   J. Naughton, A. F. Lee, S. Thompson, C. Vinod and K. Wilson, *Physical Chemistry Chemical Physics*, 2010, **12**, 2670-2678.

16.   F. Delbecq and P. Sautet, *Journal of Catalysis*, 1995, **152**, 217-236.

17.   U. Diebold, J. M. Pan and T. E. Madey, *Surface Science*, 1995, **331**, 845-854.

18.   E. Bauer, *Zeitschrift fur Kristallographie*, 1958, 372.

19.   C. Xu, X. Lai, G. W. Zajac and D. W. Goodman, *Physical Review B*, 1997, **56**, 13464-13482.

20. P. Stone, R. A. Bennett, S. Poulston and M. Bowker, *Surface Science*, 1999, **433**, 501-505.

21. K. Oura, A. A. Saranin and A. V. Zotof, *Surface science: an introduction*, Springer Berlin, 2003.

22. A. Pimpinelli and J. Villain, *Physics of crystal growth*, Cambridge university press Cambridge, 1998.

23. J. Venables, *Introduction to surface and thin film processes*, Cambridge University Press, 2000.

24. C. Argile and G. Rhead, *Surface Science Reports*, 1989, **10**, 277-356.

25. V. Di Castro and S. Ciampi, *Surface science*, 1995, **331**, 294-299.

26. A. Atrei, G. Rovida, M. Torrini, U. Bardi, M. Gleeson and C. J. Barnes, *Surface science*, 1997, **372**, 91-99.

27. A. Carley and M. Roberts, *Proceedings of the Royal Society of London. A. Mathematical and Physical Sciences*, 1978, **363**, 403-424.

28. T. E. Madey, J. T. Yates Jr and N. E. Erickson, *Chemical Physics Letters*, 1973, **19**, 487-492.

29. J. H. Scofield, *Journal of Electron Spectroscopy and Related Phenomena*, 1976, **8**, 129-137.

30. D. R. Penn, *Journal of Electron Spectroscopy and Related Phenomena*, 1976, **9**, 29-40.

31. Z. Chang and G. Thornton, *Surface science*, 2000, **459**, 303-309.

Chapter 5 – Summary and Outlook

Contents

5   Introduction

The reactivity of different Pd/Pt loaded TiO_2 catalysts towards their ability to produce hydrogen in the photocatalytic methanol reforming reactions, were probed in detail in chapters three. More specifically, the effect their weight loading, phase of reaction and phase of the titania support had on the rate of reaction. Chapter four reported the surface activity of a Pd (110) single crystal towards the behaviour of adsorbed oxygen and crotonaldehyde at ambient and high temperatures. This chapter also included details of metal vapour deposition technique used to build a model Pd/TiO_2 (110) catalyst. This chapter presents a summary of important results and conclusions from the previous results chapters, as well as an outlook on potential future work.

5.1   Summary

5.1.1   Photocatalytic Hydrogen Production

Several topics were investigated in chapter three towards hydrogen production by photocatalysed reforming of methanol, mainly the effect of metal weight loading on the titania support and the dependence of the crystallite phase of the titania pre-cursor.

The palladium/platinum weight loading dependence in the gas and liquid phase showed that independent of the phase of reaction, the amount of hydrogen produced from methanol reforming irradiated by UV light decreased for increasing metal weight loading. Additionally the gas phase reaction was found to be a more efficient environment to facilitate the methanol reforming reaction than the liquid phase, where platinum demonstrated higher hydrogen evolution in the liquid phase compared to palladium in the liquid phase but the reverse observation was seen in the gas phase reactions.

Following this the reactivity of rutile and anatase phase titania supported palladium/platinum catalysts were tested for their ability to produce hydrogen in the methanol reforming reaction, both phases were found to be poor photocatalysts alone but upon combination both chemically in the P25 based catalysts and in physical mixtures, where Pd was present on only the rutile phase, the amount of hydrogen produced was improved. This observation along

with previous findings in the group was used to propose a refined mechanism for the methanol reforming reaction occurring at the surface of the Pd/Pt TiO_2 catalyst. Highlighting the importance of both rutile and anatase phases being present at the actives sites, where hydrogen evolution occurs at the surface of the catalyst surface.

Finally, the photocatalytic system was tested for its ability to produce hydrogen using a different sacrificial organic agent, crotonaldehyde, and these results showed no activity, which could be a result of the double bond present in crotonaldehyde poisoning the catalyst surface, preventing hydrogen evolution from occuring.

5.1.2 Surface Science of Pd (110) and Pd/TiO$_2$(110)

The surface reactivity of Pd (110) was studied in chapter four, in particular that of oxygen adsorption and its behaviour once adsorbed on the well-defined surface. Oxygen was found to dissociatively adsorbed onto the surface of the Pd (110) crystal An initially high sticking probability was recorded on the Pd surface following the initial exposure to an incident beam of O_2 which dropped dramatically following a brief interruption in the incident beam. As the interruption between beam exposure points was increased the initial sticking probability increased, encroaching upon the initial sticking probability observed at the beginning of the experiment. These measurements were repeated for different reaction temperatures and different Pd anneal temperatures. It was proposed that migration of adsorbed oxygen atoms into the bulk of the crystal was happening more quickly at higher experiment temperatures, exposing more surface sites for adsorption to occur.

The reactivity of crotonaldehyde on the Pd (110) was also reported in chapter four. Crotonaldehyde was chosen to study due to the presence of a double bond and aldehyde group in this simple organic molecule. Despite encountering difficulty reproducing the reaction, the observations recorded where in line with previous studies expectations, where decarbonylation was observed for ambient reaction temperatures and dehydrogenation at elevated temperatures.

Finally production of a model Pd/TiO$_2$ (110) catalyst was attempted by metal vapour deposition and molecular beam studies carried out on the resulting surface created. Successful palladium growth by the Volmer-Weber island growth mode were reported,

however the surface palladium concentration was too low for molecular sticking reactions to be carried out on the surface.

5.2   Outlook

To supplement the work reported in this thesis, a number of different approaches could be taken, especially with regards to the work performed on the Pd/TiO$_2$ (110) model catalysts.

Firstly on the powdered catalysis application side, more detailed experiments could be conducted into the various ratios of rutile:anatase/P25 titania loaded photocatalysts to gain a more complete understanding of the importance of the rutile/anatase phase boundary experienced in these reactions. Notably testing to see if a higher ratio of rutile titania could improve the hydrogen production rate reported in chapter three.

Various other simple compounds which contain multiple organic functional groups could be recorded for their ability to act as a replacement sacrificial agent to methanol in the photocatalysis reforming reaction. Molecules to consider would be methacrolein, crotyl alcohol and even simple organic acids, to help identify whether the presence of a double bond in the sacrificial agent is poisoning the reaction.

On the surface science side, reproducing a Pd/TiO$_2$ (110) model catalyst with a higher palladium loading, to enable molecular beam experiments to be carried out would be advantageous. Not to mention upon developing a reproducible surface on which to conduct simplified reforming reactions via molecular beam it would also be interesting to try and develop an in house UV lighting system that would not only allow one to study the fundamental reaction taking place in the powdered photocatalysis reactions but the role of light in the reaction mechanism. Insight into the development of such a device could be taken from the work conducted by Henderson et al[1].

All in all these are exciting times for the expansion of photocatalysis and its application in the world of environmental hydrogen production, one which I will continue to monitor throughout my career, no matter where it takes me.

5.3   References

1.   M. Shen and M. A. Henderson, *The Journal of Physical Chemistry C*, 2012, 116, 18788-18795.